

StimDust: A 2.2 mm³, precision wireless neural stimulator with ultrasonic power and communication

David K. Piech^{1*}, Benjamin C. Johnson^{2,3*}, Konlin Shen¹, M. Meraj Ghanbari², Ka Yiu Li², Ryan M. Neely⁴, Joshua E. Kay², Jose M. Carmena^{1,2,4**}, Michel M. Maharbiz^{1,2,5**}, Rikky Muller^{1,5**}

¹ Department of Bioengineering, University of California, Berkeley, Berkeley, CA USA 94720

² Department of Electrical Engineering and Computer Sciences, University of California, Berkeley, Berkeley, CA USA 94720

³ Department of Electrical and Computer Engineering, Boise State University, Boise, ID USA 83725

⁴ Helen Wills Neuroscience Institute, University of California, Berkeley, Berkeley, CA USA 94720

⁵ Chan-Zuckerberg Biohub, San Francisco, CA USA 94158

* co-first author; ** co-senior author

Abstract

Objective: Neural stimulation is a powerful technique for modulating physiological function of the body and directly writing information to the nervous system for brain-machine interfaces. Current clinically approved neural stimulators are battery powered and tens of cubic centimeters in size. A wireless and safe neural stimulator of mm or μm scale would enable placement of stimulators directly at stimulation sites via laparoscopy, injection, or other minimally invasive surgical techniques, opening up new treatments, use cases, and patient populations. We sought to develop a wireless neural stimulation system that minimizes implant volume and mass while maintaining controllability and safety.

Approach: We present a complete wireless neural stimulation system consisting of a 2.2 mm³ wireless, batteryless, leadless implantable stimulator implant (the “mote”), an ultrasonic wireless link for power and bi-directional communication, and a hand-held external transceiver. The mote consists of a stimulator integrated circuit (IC), which performs high-efficiency ultrasonic power harvesting, decodes stimulation parameter downlink data, and generates current-controlled stimulation pulses. Stimulation parameters are time-encoded on the fly through the wireless link rather than being programmed and stored on the mote, enabling complex stimulation protocols with precise timing and closed-loop capability and without the need for on-chip memory and power consumption. Uplink data indicates whether or not the mote is currently stimulating and is encoded by the mote via backscatter modulation and demodulated at the external receiver. We characterize system power, stimulation performance and acoustic link robustness

under misalignment. We implant the mote on the sciatic nerve of anesthetized rats and investigate the full range of physiological responses achievable with the wireless system.

Main Results: The system has an implantable mote volume of 2.2 mm^3 , an 18x improvement over the state of the art for a precisely controllable current stimulator. The system performed stimulation at up to 70 mm depth in ultrasound gel. Current-mode stimulation is delivered at up to $400 \mu\text{A}$ and up to 5 kHz pulse repetition frequency, with dynamically programmable stimulation waveform timing. The mote has a wide ultrasound acceptance angle which enables operation within a 50° orientation cone and lessens the need to carefully control mote orientation during implantation. When implanted on a rat sciatic nerve and powered from outside the animal, the system elicited precisely controlled and repeatable compound action potentials. The recruitment of fibers was controlled via stimulation current and pulse width, with each parameter able to generate a full sigmoidal recruitment curve. Varying pulse repetition frequency generated differing regimes of muscle activation, including tetanus and potentially nerve block.

Significance: This system demonstrates an extremely efficient, versatile, and clinically-translatable architecture for minimally-invasive wireless neurostimulation implants which provides collective best-in-class performance in volume (2.2 mm^3), depth-to-volume ratio (32 mm^2), peak chip efficiency (82%), and overall power efficiency from wireless power at the device to electrical stimulation (2.1%). To our knowledge, we demonstrate the smallest implementation of a precision neural stimulator to date, and the design can be scaled down further to a 0.7 mm^3 mote volume with no architectural or expected performance changes. The system sets a new standard in the growing area of ultrasonically driven implants intended for minimally invasive insertion and continuous operation.

1. Introduction

Extracellular electrophysiological stimulation is broadly applied to targets in the peripheral and central nervous system and has a long history of application both in neuroscience and clinical therapies. In the peripheral nervous system (PNS), the technique is well established for treatment of chronic pain [1] and reinnervation of auditory sensory afferents with the cochlear implant [2]. More recent work has focused on creating devices that directly stimulate the PNS to regulate physiological functions [3]. For example, PNS stimulation can be used to manage blood pressure [4], rheumatoid arthritis [5], incontinence [6], and sexual function [7], reinnervate tactile sensory afferents [8], reinnervate motor efferents to directly control muscles [9] and modulate immune system function such as inflammation through the vagus nerve [10], among others.

Electrical stimulation of central nervous system (CNS) targets is well established for treatment of central motor disorders such as deep-brain stimulation (DBS) for tremor in Parkinson's disease [11]. Recent work shows promising results for: treatment of depression [12] [13], epilepsy [14], Tourette syndrome, traumatic brain injury (TBI) and obsessive-compulsive disorder (OCD) [15], modulation of decision making [16] and reward pathways [17] with applications to motivation, anxiety and addiction, restoring vision [18], improving retention of short-term memory [19], and modulating glucose metabolism with implications for diabetes treatment [20]. Intracortical microstimulation can provide tactile and proprioceptive feedback in brain-machine interface tasks [21] [22] [23] and, with training, can be used to learn a de-novo information input stream [24].

The application of clinical peripheral nerve stimulators to therapies that target nerves that are very small or deep in tissue is currently limited by the size of the implant, the risk of the implantation, and the longevity of the device-tissue interface. Current clinically deployed neural stimulators have a volume greater than 10 cm^3 [25] [26] [27]. A stimulator that is a few millimeters in size, comparable to a grain of sand, would reduce tissue trauma during implantation, reducing immune response to the implant, and it would enable ultra-minimally-invasive delivery methods such as laparoscopy or injection. A consequence of the currently large stimulators is that they must be placed in suitably large anatomical pockets. These pockets can be far from the site of stimulation (e.g., subclavical to subthalamic nucleus) or require removing substantial soft tissue or bone to form a pocket (Neuropace RNS). Long leads are required from the stimulator housing to the site of stimulation, which is a major source of infection, efficacy loss, and device failure [28], and which suffer from electromagnetic interference, crosstalk, and power inefficiencies. A stimulator the size of a grain of sand could be placed directly at the site of stimulation rather than requiring leads, both improving safety and substantially increasing the potential anatomical sites of stimulation. Peripheral nerve cuffs which are wired have been shown to cause detrimental effects to nerve function due to strain [29], emphasizing the benefit of a completely untethered device. Additionally, some new neural stimulation techniques take a connectomic approach to activity modulation, which may benefit from stimulation in multiple anatomic locations [12], thus motivating a system of many tiny stimulators rather than a single large one.

A key challenge in developing mm-scale stimulators is wireless power and communication that provides well-controlled, therapeutically relevant effects. The smallest volume stimulators have been implemented with passive components, providing inefficient voltage-mode stimulation that is sensitive to received power and electrode impedance [30] [31]. Furthermore, these stimulators do not have an uplink, preventing error detection or state monitoring via feedback to the external controller. Accurate and precise control of stimulation intensity is important for targeting a repeatable population of cells and

maintaining safety over chronic use. Active neurostimulators employing integrated circuits can use active rectifiers to achieve a higher power conversion efficiency and deliver current stimulation that is independent of received power [32] [33] [34]. However, most active neurostimulators rely on a recovered clock from the wireless signal as well as programmed registers to generate stimulation waveform timing. This results in significant power overhead and limits the dynamic programmability of the waveform. Furthermore, most of these wireless systems use electromagnetic (EM) energy for power and communication, which couples inefficiently at cm scales deep within tissue [35].

Recently, ultrasound has been proposed as an efficient way to power and communicate with mm-scale implants deep in tissue [36], resulting in significant volume reduction for implants [37] [38] [39] [40]. Compared to EM at 2 GHz, ultrasound energy at 2 MHz has less attenuation through tissue (1-2 dB/cm vs. 9 dB/cm), a higher FDA limit (7.2 mW/mm² vs. 0.1 mW/mm² [41]), and a smaller wavelength (0.75 mm vs. 25 mm) for more efficient coupling to small implants.

Here, we present a system for wireless neural stimulation that employs 2.2 mm³ leadless, wireless “StimDust” stimulation motes. The ultrasonically powered StimDust motes contain a state-of-the-art custom integrated circuit (IC). A single link from the external transceiver to the mote provides power and bidirectional communication, reducing volume. A custom wireless ultrasonic protocol dynamically sets stimulation waveforms, drastically reducing the power consumption of the StimDust motes while maintaining a high degree of timing control and precision. In section 2, we describe the design and fabrication of the full system, including the IC, the custom interrogator, the communication protocol, and the mote. In section 3, we characterize performance across the full range of possible stimulation parameters, measuring power consumption and bidirectional communication performance to understand the effect of crucial, often under-reported, real-world non-idealities including acoustic link misalignment. Section 3 also provides *in vivo* data of wireless stimulation in the rat sciatic nerve with a fully implanted mote across a range of physiologically relevant parameters. Finally, discussion and conclusions are given in section 4.

2. System design, fabrication and methods

2.1. System overview

Figure 1 gives a conceptual overview of the StimDust system and its implementation. An external transceiver (section 2.4) (figure 1(e)) established an ultrasonic wireless link through body tissue to an implanted StimDust mote. A single ultrasonic link provided both power to the mote and bidirectional communication. The mote consisted of a piezoceramic as the ultrasonic transducer, a custom IC for power

rectification, communication, and stimulation (section 2.2), a discrete capacitor for energy storage, bipolar stimulation electrodes, and a nerve cuff integrated on a thin polyimide printed circuit board (PCB). The mote was surgically implanted directly at the stimulation site, in this case the rat sciatic nerve (figure 1(b)), the wound was closed (figure 1(d), note that the transcutaneous wires seen here are optional test leads), and the external transceiver was coupled to the outside surface of the body with ultrasound gel. The system could produce a broad set of clinically relevant stimulation currents, pulse widths, and pulse repetition frequencies (PRF); these were sufficient to elicit compound action potentials (CAPs) in the sciatic nerve, compound muscle action potentials (CMAPs), and associated twitches in downstream muscles.

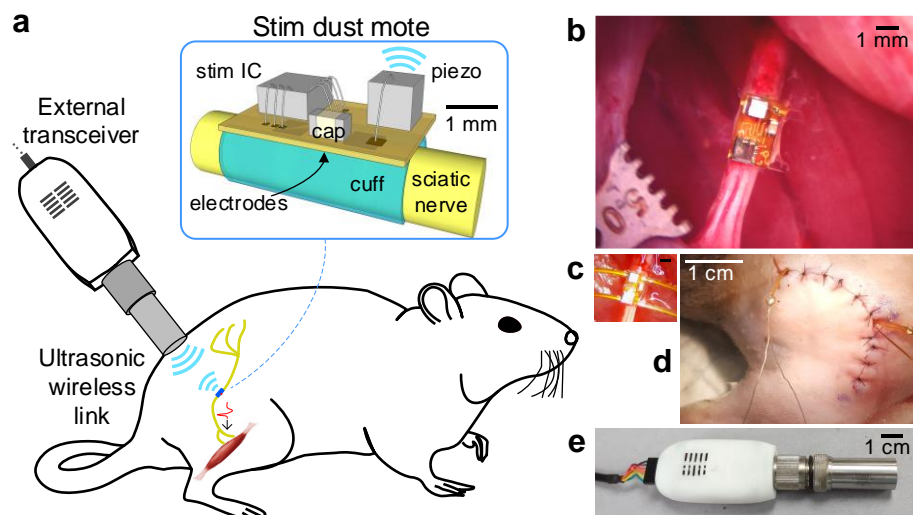


Figure 1: 'Stim dust' wireless neural stimulator system overview: (a) Cartoon depicting the stim dust setup, with this preparation for stimulation of the sciatic nerve of a rat. (a detail) The major components of the stimulating mote. (b) The stimulating mote is fully implanted and affixed to the sciatic nerve. Stimulation pulses from the mote elicit compound action potentials in the nerve and compound muscle action potentials in the hindlimb musculature. (c) Optional test leads on the mote are used for diagnostic and data reporting purposes to measure internal signals on the mote. They provide no power or control signals to the mote, and the mote functions with these leads disconnected from all external instrumentation. (d) The wireless link traverses skin and muscle on top of a closed surgical site, here at the hindquarters of the animal above the sciatic nerve. (e) The external transceiver establishes an ultrasonic wireless link with the mote. The power and data cable is on the left and the external transducer is on the right.

A functional block diagram of the system is detailed in figure 2. The external transceiver (figure 2, left) (section 2.4) utilized a microcontroller to synthesize a low-voltage transmit signal, which encoded downlink stimulation parameter for each pulse onto a 1.85 MHz carrier. The low-voltage transmit signal from the microcontroller was stepped-up in voltage and drove the external piezoelectric ultrasound transducer (figure 2, bottom). During the 'off' periods of the transmit signal, the external transceiver

toggled from Tx (transmit) to Rx (receive) mode to capture and demodulate uplink data from the acoustic signal backscattered by the mote.

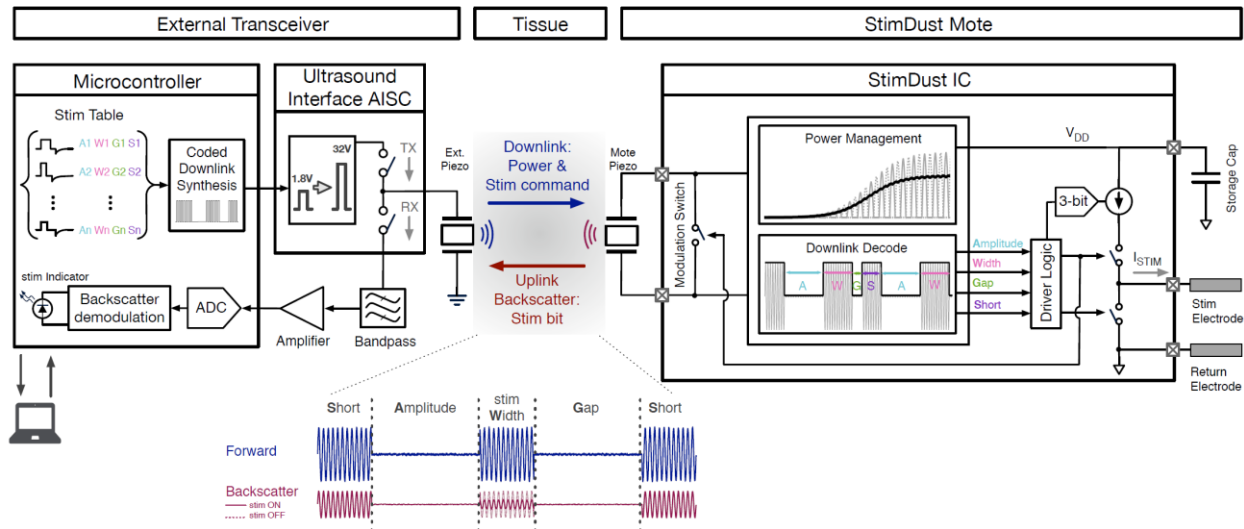


Figure 2: System block diagram: (left top) The external transceiver transmits a downlink ultrasound pattern which provides power and stimulation data to the mote. Stimulation parameters are set by the user and stored in a stim table, which holds information for up to 4500 repeating stim events. The coded downlink ultrasound waveform is first synthesized with serial outputs and on-chip timers, then stepped up to the ultrasound drive voltage (up to 32 V) which drives a transducer. (bottom left) The downlink ultrasound waveform encodes stimulation current amplitude [A], stimulation pulse width [W], interphase gap duration [G], and electrode shorting duration [S] with an on-off-keyed time-delay code. (right) The mote harvests power and decodes stim parameters from the downlink, and applies the stimulation pulse to the tissue. Power management circuitry rectifies the piezo voltage, stores energy in an off-chip cap, regulates supplies, and extracts the envelope of the coded downlink waveform. A finite state machine uses the envelope and a clock signal derived from the piezo waveform to drive the stimulator with the correct amplitude and timing provided by the coded downlink. During stimulation, a modulation switch is activated, changing the reflectance of the mote piezo. (bottom left) A reflected signal carries state information in amplitude modulation of the stim pulse region of backscatter. (left) During the ‘off’ portions of the on-off keyed coded downlink, the external transceiver digitizes the reflected wave. By comparing two regions, amplitude modulation applied by the mote is detected, confirming that stimulation has occurred.

The implanted mote used an IC (section 2.2) to rectify energy harvested by the mote’s piezo. Energy harvested by the IC was stored in an off-chip capacitor to ensure consistent operation of the IC during the ‘off’ cycles. The IC decoded received ultrasound to determine stimulation current amplitude, pulse width, interphase gap, passive recharge time, and inter-pulse interval. During stimulation, the IC modulated the impedance across the piezo to change the amplitude of the reflected wave. This indicated to the external transceiver that the IC is stimulating and operating properly.

2.2. Design of the StimDust IC

The objective of the IC design was to provide a well-controlled current-mode stimulus independent of variations in electrode impedance and piezo voltage while efficiently using energy harvested from the piezo [42]. Furthermore, the IC’s functionality was designed to not be heavily dependent on the

electromechanical specifications of the piezo, such as resonant frequency or ring down time. This was to make the IC compatible with piezocrystals of various sizes and permits tuning of the carrier frequency without disrupting IC functionality.

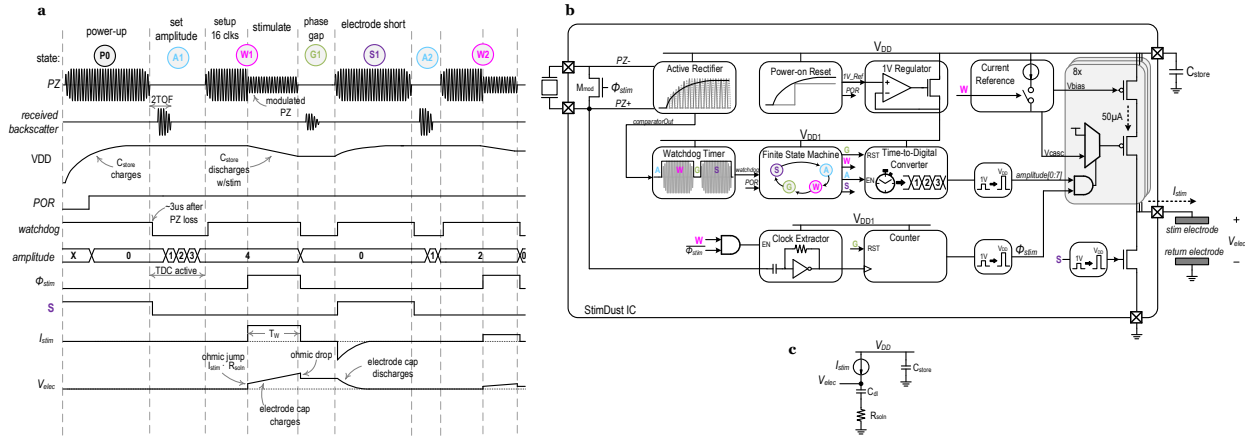


Figure 3: StimDust IC: (a) The timing diagram with resulting stimulation waveform. **(b)** The implemented architecture that decodes the received ultrasound and generates the stimulation waveform. **(c)** The model used to determine available voltage headroom from the electrode parameters and external storage capacitor.

The IC used a custom ultrasound protocol (figure 3, left), which enabled dynamically controlled stimulation waveforms and high system efficiency while maintaining a high degree of timing control and precision. The protocol utilized the shape of the incoming ultrasound envelope to encode stimulation amplitude and system timing thereby eliminating the need for an on-chip clock to ensure timing precision. This reduced power consumption and afforded greater stimulation waveform timing flexibility compared to solutions that rely on a clock receiver, divider circuits, and on-chip registers to generate the stimulation waveform [43] [32]. As shown in figure 3, an initial power-up sequence charged the implant's storage capacitor, C_{store} . For this work, the power-up sequence was on the order of 300 ms; this ensured that power-up time was several time constants (16 ms) of the piezo series resistance (4 k Ω) and the storage capacitance (4 μ F). As the supply voltage of the IC (V_{DD}) ramped up to 2.5 V, a power-on-reset (POR) signal (triggered at 1.6 V nominally) was generated to initialize the chip. If the POR signal was not generated, or V_{DD} dropped below the reset level, the IC would not stimulate. This was a fail-safe against aberrant stimulation if the system were to lack sufficient power. A linear voltage regulator was used to power the digital circuitry at $V_{DD1} = 1$ V to lower the dynamic switching power consumption ($P_{dyn} \propto CV_{DD1}^2f$).

In addition to a power-up sequence, the protocol was comprised of 4 repeating states: (A): set amplitude, ultrasound off; (W): pulse width, ultrasound on; (G): interphase gap, ultrasound off; (S): shorting/recharge phase, ultrasound on. The A and G states are called ultrasound-free intervals (UFI). All of these states encoded information pertinent to the stimulation waveform interpreted by the IC. The first state (A) occurred during the first ultrasound-free interval (UFI) and encoded the stimulation amplitude. A

watchdog timer circuit on the IC detected the UFI approximately 3 μs after the ultrasound is off. This triggered a 3-bit time-to-digital converter (TDC), where each level was approximately 8 μs and was easily calibrated to account for die-to-die variations by using the external transceiver to perform a one-time sweep of the width of region A and measuring output current. The 3-bits of the TDC were stored in memory for the amplitude of the stimulation pulse.

When ultrasound returned, ending the first UFI and beginning state W, a pre-stimulation setup sequence began. The clock extractor was enabled and fed the 4-bit counter. During this time, the current reference circuitry was enabled and the 16-cycle setup sequence allowed it to settle prior to stimulation. Note that the clock extractor and current reference circuitry consumed significant power, so they were heavily duty-cycled and only used during the 16-cycle setup sequence and during stimulation respectively. On the 16th cycle, stimulation was enabled by the output of the counter, Φ_{stim} , which controlled a cascode switch that mirrored out the reference current according to the amplitude set by the TDC.

The stimulation pulse width, T_w , continued for the remaining duration of the third state (W) after the setup sequence completed. For this reason, the pulse width was controllable with a timing resolution of $1/f = 540 \text{ ns}$. When stimulating, current flowed from the stimulation electrode to the return electrode. In order to avoid compliance limiting the current stimulator, the V_{DD} of the IC required sufficient compliance voltage to be able to accommodate the voltage rise across the electrode ($V_{\text{elec}} = I_{\text{stim}} \cdot R_{\text{Soln}} + I_{\text{stim}} \cdot T_w / C_{\text{dl}}$) while the supply voltage dropped from stimulation current discharging the storage capacitance ($V_{\text{DD}} = 2.5 - I_{\text{stim}} \cdot T_w / C_{\text{store}}$). Thus, to keep the stimulator operating properly ($V_{\text{DD}} > V_{\text{elec}}$), it was important to keep the electrode impedance low (section 2.3) and to use a large charge storage capacitor on the supply node. Since the mote was backscatter modulating during stimulation, incoming ultrasound could not be used to charge the mote during this period.

At all times when the ultrasound was on, a fraction of the incident ultrasonic energy was reflected back to the external transceiver. The amplitude of the reflected wave detectable at the transceiver was a function of the electrical load of the mote piezo. The delay seen by the transceiver between emission and detection of the reflected energy was twice the acoustic time-of-flight between the external transducer and the piezo. During stimulation, a transistor switch, M_{mod} , was turned on to create a weak short ($\sim 4 \text{ k}\Omega$) across the piezo terminals, reducing the amplitude of the reflected (i.e. backscattered) signal. When M_{mod} was off, the electrical load impedance across the piezo ranged from 10 $\text{k}\Omega$ to 300 $\text{k}\Omega$ depending on the power consumption of the IC. Regardless of the level of power consumption, the increased electrical load impedance resulted in an increase in the amplitude of the reflected energy. The impedance change during the stimulation provided a 1-bit data uplink and safety indicator so that the external transceiver knows the mote was stimulating.

Stimulation was terminated at the second UFI. In this state (G), the chip was in standby mode. The stimulation electrode was tri-stated and accumulated charge remained on the electrode interface, creating an interphase gap. Interphase gaps have been shown to decrease stimulation thresholds in auditory nerves, motor nerves, and retinal ganglion cells, in addition to decreasing perceptual thresholds in cochlear implant patients and epiretinal prosthesis patients [44] [45]. The interphase gap duration was controlled directly by length of the UFI. The minimum interphase gap to ensure proper state transition was roughly 6 μ s and was set by the combination of the watchdog circuit's time constant and piezo ring-up and ringdown. The mote's maximum interphase gap was limited by the charge stored on the capacitor and is approximated as

$$T_{\max} = C_{\text{store}} * \Delta V / I_{\text{standby}}$$

where ΔV is the acceptable voltage drop on V_{DD} and I_{standby} is the current consumption of the IC in standby (roughly 1.6 μ A). Note that ΔV must also consider the voltage drop that occurred during stimulation since the storage capacitance has not been recharged. With a 4 μ F C_{store} in this work, the maximum interphase gap was typically greater than 1 second, substantially more than the physiologically relevant range between 0 and 2 ms.

The end of the second UFI put the IC into the fourth state (S). During this state, received ultrasound recharged the storage capacitance and the IC shorted the stimulation electrode to ground, clearing the stimulation charge that was stored on the electrode. Given the impedance of the electrodes used in this work (section 2.3), the residual stimulation charge was cleared within a few milliseconds. For this reason, passive recharge at the tissue-electrode interface [46] was favorable to conventional biphasic stimulation since it consumes half the energy without limiting stimulation frequency. Furthermore, biphasic stimulators typically use an additional shorting phase to clear residual charge that accumulates from phase mismatch.

By using low-impedance electrodes (<6.25 k Ω , detailed in section 2.3) and limiting the drop on V_{DD} by using a large storage capacitance (4 μ F), we could operate with a nominal V_{DD} of 2.5 V – 3 V. This reduced the instantaneous stimulation power ($V_{\text{DD}} \cdot I_{\text{stim}}$), and enabled the use of a standard CMOS process. The IC was fabricated in a TSMC 65nm LP CMOS process and occupied an area of 1 mm² with a profile of approximately 250 μ m (figure 4(a)). The active area was 150 μ m x 400 μ m. 2.5V I/O devices were used for the stimulator circuitry and active rectifier while 1.2V core devices were used for the digital control circuitry.

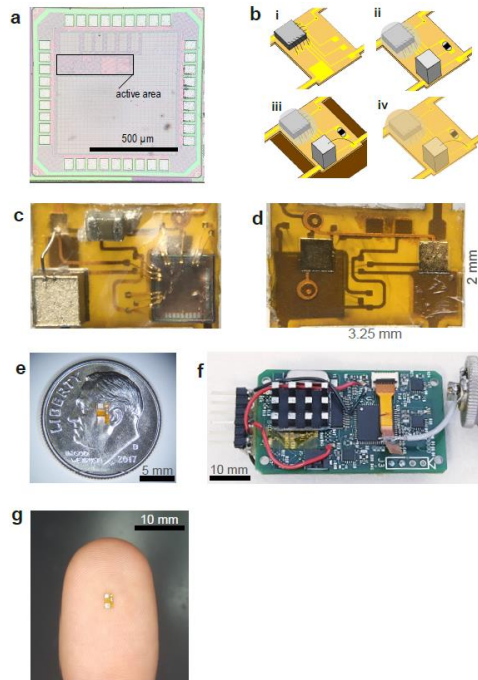


Figure 4: Stim dust mote fabrication: (a) Mote IC die photo. (b) Mote fabrication steps: (i) IC die is wire-bonded to mote flex substrate (ii) discrete capacitor and piezo are bonded with silver epoxy, and die is encapsulated with epoxy (iii) piezo is wire-bonded (iv) mote is encapsulated with parylene. (c) Top view of mote: piezo on left, capacitor at top, IC on right. (d) Underside view of mote: ground electrode on left, working electrode on right. (e) Size comparison to US dime. (f) External transceiver board. Data and power connection is on the left, microcontroller is under the passive heat sink, ultrasound interface chip is middle-right and transducer connector on the right. (g) Size comparison with mote on a finger.

2.3. Design, fabrication, and assembly of the StimDust motes

The StimDust motes were built on a 100 μm thick, polyimide, flexible PCB (Altaflex, Santa Clara, CA). Polyimide substrates were preferable to FR-4 substrates due to the higher thermal budget, superior chemical compatibility with organic solvents, and higher flexibility of the substrate, facilitating device testing and *in vivo* implantation.

To prevent compliance limiting when using the full current range of the chip, the electrode impedances were designed to be $< 6.25 \text{ k}\Omega$ at the stimulation pulse frequency (2.5 kHz for a typical pulse width of 200 μs). The impedance of the gold electrodes on the PCB was lowered by electroplating poly(3,4-ethylenedioxythiophene) polystyrene sulfonate (PEDOT:PSS) using a NanoZ impedance testing and electroplating device (White Matter LLC, Mercer Island, WA). In recent work, PEDOT:PSS has demonstrated a charge injection limit 15x that of PtIr and IrOx electrodes and $>3\text{x}$ reduction in the voltage transient [47]. The impedance of the gold stimulation electrodes was characterized in 1x phosphate buffered saline (PBS) using a NanoZ before and after PEDOT plating and again after full assembly of the motes. One electrode served as the active electrode while the other served as the reference electrode. A frequency sweep between 1 Hz and 5.02 kHz was performed and the impedance data collected, yielding an impedance of approximately 4 k Ω at 2.5 kHz (the pulse in this study with the lowest frequency and therefore highest impedance) [42].

Following electroplating, the IC was attached to the PCB using a conductive silver epoxy (H20E, Epotek, Billerica, MA) (figure 4(b)) and cured at 150° C for 10 minutes. The ASIC and PCB were then cleaned in

acetone, followed by isopropyl alcohol and DI water to clean the device prior to wirebonding. The IC was wirebonded to the PCB using an ultrasonic wedge wirebonder (7400B, West Bond, Scotts Valley, CA) and potted in UV-curable epoxy (AA 3526, Loctite, Düsseldorf, Germany) to protect the wirebonds.

Next, a 750 μm x 750 μm x 750 μm lead-zirconate titanate (PZT) cube (841, APC Int., Mackeyville, PA) and an 0201 surface mount capacitor for charge storage were attached to the PCB using silver epoxy and cured at 150° C for 10 minutes. The PZT coupon was diced from a 750 μm thick sheet of PZT (841, APC Inc.) using a wafer-dicing saw with a ceramic-cutting blade. The PZT was purchased with its terminals premetallized with 12 μm of fired-on silver. To complete the circuit, the top contact of the PZT coupon was wirebonded to the PCB.

The devices were then coated with roughly 10 μm of parylene-C for insulation using chemical vapor deposition (Specialty Coating Systems, Indianapolis, IN). Parylene was chosen as the insulation material due to its excellent properties as a moisture and chemical barrier [48]. Furthermore, because parylene can be precisely deposited with thicknesses on the order of microns, it did not damp the vibrations of the piezoceramic as strongly as other insulation materials such as polydimethylsiloxane (PDMS) or epoxy. The stimulation electrodes were exposed by gently scoring the parylene around the electrodes using a tungsten probe tip and peeling the parylene away. The parylene encapsulation used in this work is expected last from several months to low-years in the biological environment [49]. Implementation of recent advances for long-term conformal encapsulation for mm-scale implantable devices should enable decades- or lifetime-longevity [50] [51].

The completed StimDust mote had maximal dimensions of 3.1 mm length, 1.9 mm width, and 0.89 mm height. The mote volume was 2.2 mm³, the convex hull volume was 3.6 mm³, and the rectangular bounding box volume was 5.3 mm³. For comparison, current deep brain stimulation electrodes are 1.27 mm in diameter and several centimeters in length [25]. A more aggressively scaled mote was also designed which used the same system architecture, piezo size, and fabrication techniques, and which had no expected difference in performance. For this design, an IC was fabricated with its size reduced by removing unnecessary test circuits and debug pads and using pad-over-circuit. Additional size reduction in the mote design came from the use of a 0.5 mm x 0.25 mm footprint storage capacitor and refinement of component and wirebond placement. While this smaller design was not used for the experiments reported in this paper, it did achieve a size with maximal dimensions of 1.17 mm length, 0.77 mm width, 0.89 mm height, 0.61 mm³ volume, 0.7 mm³ convex hull volume, and 0.8 mm³ rectangular bounding box volume (data not shown). This design is substantially smaller than the tip of a DBS lead.

To aid in surgical placement of the mote on the rat sciatic nerve, a cuff was added. The cuff was made by cutting a small piece of silicone tubing (0.8 mm ID, 1.6 mm OD) to roughly the length of the mote. The

tubing was then cut in half and attached next to the electrodes using UV-curable epoxy and silicone adhesive.

2.4. Design of the external transceiver

The external transceiver was a compact device designed to be held by a user such that an ultrasonic transducer head is held against the skin of a subject. A previous version demonstrated that the external transceiver could also be configured as a wearable device with a low-profile transducer [52]. The transceiver established an ultrasonic wireless link with the mote to provide power, control stimulation parameters via time-coded downlink data, and report back whether the mote has successfully applied each stimulation pulse via detecting backscatter modulation. It was designed around two major components: a high-performance microcontroller (NXP LPC4370) for system control and digital modulation / demodulation, and a custom ultrasound interface IC [53]. Due to the relatively low frequencies used, a full-digital transceiver was implemented with direct digital synthesis of the transmit signal and digitization of the raw receive signal, enabling greater modulation / demodulation design flexibility.

Signal flow through the transceiver is depicted in figure 2. A stimulation protocol was programmed into the system and stored in a stimulation table as a sequence of A, W, G, S duration values for each stimulation event. This table could store up to 4500 unique stimulation events of differing parameters and is repeated. An on-board PLL generated a 1.85 MHz square wave carrier signal and on-board timers utilized the stimulation table data to encode the downlink timing with on-off keying onto the carrier signal with sub-microsecond precision. The ultrasound interface IC used a high-voltage rail provided by an external power supply (5 to 36 V) to level-shift the low voltage transmit signal from the microcontroller to a high-voltage signal used to drive the external piezoelectric ultrasound transducer. Two different ultrasound transducers could be alternately used: one for interfacing with motes at shallow depth (12.7 mm diameter, 21.6 mm focal length, V306-SU-F0.85IN-PTF, Olympus NDT, Waltham MA), and one for interfacing with deep motes (25.4 mm diameter, 47.8 mm focal length, V304-SU-F1.88IN-PTF). For *in vivo* tests using these commercial, metal-encased transducers, a thin sheet of latex was stretched over the transducer face and castor oil was used as coupling between the transducer face and the latex. This prevents electrical paths from the stimulation site to ground through the transducer casing. The electromechanical frequency response of the transducer filtered the square wave transmit signal resulting in a sinusoidal acoustic-domain signal. A single-element external transducer was chosen due to the ease and selection of commercial-off-the-shelf options. Depending on the clinical use case, a wearable external transceiver with a multi-element low-profile external transducer, as demonstrated in [52], may enable

more convenient long-term stimulation and beamforming for fine-tuning of the beam axis relative to the mote position [54].

During UFI (states A and G), the ultrasound interface chip switched from transmit (Tx) to receive (Rx) mode to pick up the backscattered signal captured by the external transducer. The receive signal was band-pass filtered and amplified (LT6203) by 4.8 dB. A 12-bit ADC on the microcontroller digitized the receive signal at 17 MSPS. The digitized backscatter was broken into two regions based on the timing values of the downlink modulation signal. The first backscatter region, $x_{S,n-1}$, was captured immediately after the transceiver $S_{n-1} \rightarrow A_n$ transition and had a duration of twice the acoustic time-of-flight (TOF) between the external transducer and the mote ($\sim 20 \mu\text{s}$ to $60 \mu\text{s}$ depending on mote depth). This corresponded to the duration when the external transducer was no longer driven, but the acoustic wave was still travelling down to and reflecting off the mote. The $x_{S,n-1}$ region had an amplitude dependent on the mote modulation state during the mote S period, which corresponded to the mote M_{mod} off. The second backscatter region, $x_{W,n}$, was captured immediately after the transceiver $W_n \rightarrow G_n$ transition and also had a duration of two TOF. This region had an amplitude dependent on the mote modulation state during the mote W period. When the mote was fully powered and properly stimulating, M_{mod} was on during this region, otherwise M_{mod} was off. When turned on, M_{mod} reduced the electrical impedance seen by the piezo, reducing the amplitude of the backscattered wave.

To detect the modulation or uplink data for each pulse n (d_n), the normalized difference between the time-integrated amplitudes (L1 norms) of the $x_{W,n}$ and $x_{S,n-1}$ backscatter signals were compared to a threshold.

$$d_n = \frac{\|x_{W,n}\|_1 - \|x_{S,n-1}\|_1}{\|x_{S,n-1}\|_1} < \text{thresh}$$

The normalization canceled out any variation due to downlink power or path loss. With calibration, a threshold was determined which separates the backscatter relative difference into “1” bits below the threshold and “0” bits above the threshold. This single-bit backscattered data from the mote, which signified whether the mote was stimulating or not, was given as feedback to the operator of the handheld external interrogator via an LED when the mote was detected as active. The backscatter bit and raw backscatter digitized waveforms could also be streamed to a PC via a serial connection for further logging and diagnostics, though this was not necessary for normal operation (backscatter data presented in the figures came from this offload connection).

2.5. Characterization of motes in ultrasound gel tissue phantom

To assess performance of the system, a mote with test leads was placed in ultrasound gel (Aquasonic Clear, Parker Labs, Fairfield NJ), either freely-floating or mounted on top of a 700 μm diameter steel rod connected to a rotation stage (RP01, Thorlabs, Newton, NJ). Bubbles were removed from all ultrasound gel used in this study via centrifugation for 16 minutes at 428 x g to 1052 x g. Ultrasound gel has acoustic impedance and attenuation within 0.7% and 1.9%, respectively, of those of water [55]. An electrical load was attached to the mote electrode terminals to mimic tissue electrical properties (series 3 k Ω and 22 nF were used; note that in-vivo values were $\sim R_{\text{Soln}} = 4.54$ k Ω and $\sim C_{\text{dl}} = 17.9$ nF). The external transceiver was mounted to a computer-controlled 2-axis stage (XSlide, VelMex) with the external transducer contacting the gel. Mote parameter encoding and decoding performance were assessed at a mote depth of 18 mm using the 12.7 mm diameter external transducer at a transmit voltage of 19.4 $V_{\text{pk-pk}}$. Stimulation, power and backscatter performance were assessed at a mote depth of 48 mm using the 25.4 mm diameter external transducer at a transmit voltage of 25.6 $V_{\text{pk-pk}}$. The performance of the system at various positions and alignments of the mote in the acoustic link were assessed by rastering over the transverse translational and angular offset dimensions at a depth of 48 mm. The performance of the system at various depths and at high pulse repetition frequency were assessed with the mote on the central axis of the external transducer using the 25.4 mm diameter external transducer at a transmit voltage of 31.5 $V_{\text{pk-pk}}$. The external transceiver acoustic field for each transducer was characterized in a separate experiment in a water tank using a hydrophone (HGL-0400, Onda, Sunnyvale CA USA).

2.6. *In vivo extracellular electrophysiological stimulation*

All *in vivo* procedures were performed in accordance with University of California-Berkeley Animal Care and Use Committee regulations. Wireless stimulation was performed in 4 animals. For each procedure, a male Long-Evans rat (Charles River, Wilmington, MA) of approximately 300 g was anesthetized with 1 mL per 200g of 250 g/L ethyl carbamate dissolved in sterile saline and placed on an isoflurane vaporizer at 0.5% isoflurane and 300 mL/minute flow rate. The skin around the leg was shaved and depilated. A semicircular flap incision was made from approximately the midpoint of the tibia to the midpoint of the femur, following the curvature of the knee joint. The biceps femoris was longitudinally bisected and resected to uncover the sciatic nerve. The fascia holding the sciatic nerve to the underlying musculature was removed, but the epineurium was left intact. The area was irrigated with sterile saline to ensure good electrical contact between the mote and the nerve. A mote was placed on the nerve approximately 4 mm proximal to the bifurcation of the nerve to innervate the limb extremities. The mote had 5 test leads attached to it for data collection purposes (GND, $V_{\text{pz+}}$, $V_{\text{pz-}}$, V_{DD} , V_{elec}) (figure 1(c)). These leads were unnecessary for the function of the mote and were used for debugging and recording wired data to compare with the wireless readout when characterizing the performance of the mote; they provided no

power or communication signals to the mote. To ensure that these leads had no effect on the performance of the system, they were completely disconnected from all external instrumentation during a test trial and no change in system performance was seen.

For initial verification of functional stimulation and sweeps of stimulation current and pulse width, the surgical site was left open and the external interrogator was mounted such that the external transducer face was approximately 20 mm from the mote, with ultrasound gel filling the intervening space. The external interrogator was then turned on and chip V_{DD} measured from test leads on the mote. The external interrogator position was adjusted to ensure good alignment with the mote and successful stimulation was verified with test leads on the mote. This use of a measure of V_{DD} for fine alignment of the mote was used for repeatability between trials but was not necessary for function of the system. To verify this, positioning of the external transducer relative to the mote was performed without using V_{DD} as an alignment reference and the mote was able to receive enough power to function. The backscatter amplitude was also an option to aid in positioning the mote without use of a V_{DD} measurement.

Two penetrating steel electrodes were placed in the gastrocnemius muscle to capture the electromyogram signal (EMG) induced by sciatic nerve stimulation. The EMG signal was amplified by 1000X, bandpass filtered at 10 Hz to 3 kHz (DP-304, Warner Instr. Co., Hamden CT), and digitized at 100 kSPS (NI DAQ USB 6001, NI, Austin TX).

The external interrogator was programmed to specify a certain stimulation current, pulse width, and pulse repetition frequency, and the system was initiated and performed approximately 30 to 60 stimulation events per condition before being set to different stimulation parameters. The pulse repetition frequency was kept at a relatively low $\sim 1/3$ Hz while generating recruitment curves to prevent muscle fatigue. Stimulation of the sciatic nerve elicited compound muscle action potentials (CMAP) across much of the lower leg musculature. CMAP amplitudes were calculated from baseline to the first peak. To calibrate the stimulation response curve, mote parameters were swept across stimulation current and stimulation pulse width dimensions, and baseline-to-peak CMAP amplitudes were calculated to construct a recruitment curve. A sweep of pulse repetition frequency was also performed and qualitative muscle response recorded.

To verify that the acoustic link was functional while transmitting through the tissue layer of the animal, the experiment was repeated with a closed surgical site. Excess ultrasound gel was removed, the biceps femoris replaced over the nerve and mote, and the skin incision sutured with 6-0 nylon suture. With the wound closed, ultrasound gel was applied to the outside of the animal and the external interrogator was repositioned with the external transducer in contact with gel so that the distance from transducer to mote

was 18 mm, with approximately 5 mm consisting of tissue. Downlink, stimulation, and uplink performance were then assessed with the fully implanted mote.

3. Results

3.1. Functional motes tested ex vivo operated as designed, with an average stimulation current error of 2.0%, a 2.38 - 5.05 kHz maximum PRF and a BER of 2.5×10^{-5}

In vitro testing of the system showed nominal power-up, communication and stimulation with the mote. The step response ring-up time of the external transducer was approximately 1 cycle, or 0.56 μs . The ring-up time for the external transducer and mote piezo system (full downward link) was approximately 3.5 cycles or 1.94 μs . The ring-up time for the external transducer, mote piezo, and backscatter capture system (full bidirectional link) was approximately 4.5 cycles or 2.5 μs . The error between specified current output and actual current output across all 8 amplitude levels (50 μA to 400 μA) was 2.0% on average and 8.1% maximum (maximum current error of 5.7 μA). The system achieved up to 2.38 kHz pulse repetition frequency (PRF) while stimulating with a pulse width of 80 μs at 400 μA and minimal compliance limiting. A PRF of 5.05 kHz was achieved with 50 μA current and 80 μs pulse width. At higher frequencies, and consequently higher duty cycles, there was less time to recharge the storage capacitor between pulses, resulting in an eventual V_{DD} droop and a compliance-limited current output. The maximum PRF under these conditions was 16 kHz. Dynamic programmability was demonstrated by producing pulses of differing stimulation current and pulse width in immediate succession in less than 1 ms (figure 5(a)). A pulse-train mode was demonstrated by interspersing several pulses of short-duration shorting-phase with a pulse of long-duration shorting-phase. This yielded a pulse-train every 500 ms, with each train containing 10 pulses of 100 μs pulse width occurring every 750 μs .

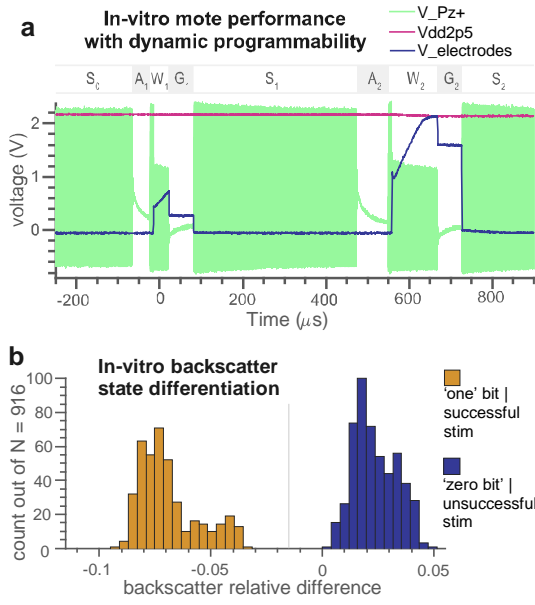


Figure 5: In-vitro Performance: (a) Mote waveforms during a representative stimulation sequence where stimulation parameters are changed on-the-fly. The first stimulation pulse at 150 μA for 37 μs is specified by regions A_1 , W_1 , and G_1 . The second stimulation pulse at 300 μA for 110 μs is specified by A_2 , W_2 , and G_2 . (b) Backscatter relative difference for 916 stimulation pulses. Successful stim pulses were achieved under good mote operating conditions and verified stim at the outputs. Unsuccessful stim pulses were captured when the power to the mote was reduced until output stimulation was no longer performed. The two populations show good separation, enabling the use of backscatter as an indicator of successful stimulation.

Piezo impedance modulation via the M_{mod} switch for uplink data modulation (figure 5(a)) showed a drastic amplitude change in $V_{\text{Pz+}}$. At the external transceiver, the measured backscatter modulation uplink performance (figure 5(b)) showed good separation between pulses with a high relative difference between the modulation states (M_{off} during S_{n-1} and on during W_n) and pulses with a low relative difference between the modulation states (M_{mod} off during S_{n-1} and W_n). The actual uplink bit error rate (BER) was 0 out of 916 using a backscatter relative difference separation threshold of -0.015. The estimated bit error rate was 2.5×10^{-5} using a Gaussian fit on each population. Using a running average of three stimulation pulses reduced the BER to 1×10^{-5} .

3.2. The system operated at as low as 142 mW/cm² peak acoustic intensity, (20% of the FDA limit for diagnostic ultrasound), and safely delivered up to 89 μW of stimulation power

The acoustic beam patterns of the 12.7 mm and 25.4 mm diameter external transducers (figure 6(e-f)) were measured to have a focal plane intensity transverse full-width-half-maximum of 1.6 mm and 1.8 mm, respectively, and an axial intensity longitudinal full-width-half-maximum of 14 mm and 17.7 mm. The minimum external transceiver transmit voltage needed to power up a mote and stimulate (using 12.7 mm diameter external transducer) was 10.5 $V_{\text{pk-pk}}$. This corresponds to a minimum necessary peak acoustic intensity at the face of the mote piezo of 142 mW/cm² and a mechanical index of 0.049 (pressure amplitude of 66.1 kPa), 20% and 2.6%, respectively, of the FDA limits for diagnostic ultrasound.

The power performance of the system was measured for two conditions: benchtop operation at high PRF and *in vivo* operation with a fully implanted mote at low PRF (table 1). V_{TX} and $P_{\text{electrical}}$ into the external transducer were measured at the output of the external power supply used to supply the ultrasound

interface chip. Acoustic domain measurements were made with a hydrophone in water. For the *in vivo* condition, the given acoustic values were de-rated from the water tank hydrophone measurements to take into account expected loss from impedance mismatches and absorption in 2 mm of skin and 3 mm of muscle [56] [57] [58]. The external transducer was heavily damped to shorten its impulse response and much of the acoustic power generated in the external transducer piezo was dumped into the absorptive backing layer, causing the electrical input power to acoustic power at the focal plane efficiency to be low. The acoustic power at the focal plane (depth of the mote) was integrated over a 1 cm radius circle, which is at least 97% of the total power in the focal plane. The face of the mote captured approximately 20% of the acoustic power in the focal plane. This was a trade-off that balances minimizing the power coupling sensitivity of small transverse misalignments with minimizing the unused ultrasound power radiating into the body.

The value for power conversion efficiency from acoustic power at the face of the mote to electrical power charging C_{store} on the mote took into account acoustic to electrical power conversion efficiency and rectifier efficiency. The P into C_{store} measurement was measured from the rate of charge of the C_{store} capacitor voltage during initial mote power-up when the mote was under power conditions in which V_{DD} reached a maximum of approximately 3 V. Under a given incident acoustic power, the mote harvested greater electrical power (as measured by P into C_{store}) when V_{DD} was low than when it was high. At 1.2 V_{DD} , the rate of electrical power harvest was maximum but V_{DD} was below the POR cutoff and the device did not stimulate. Between 1.9 V_{DD} and 3.0 V_{DD} , the mote was able to stimulate, and power harvest was moderate at 1.9 V_{DD} and decreased to 3.0 V_{DD} , which was the point where C_{store} was nearly topped off 'trickle charging' under those incident acoustic power conditions. e; The stimulation load was modeled as a solution resistance (R_{soln}) and double-layer capacitance (C_{dl}) in series. R_{soln} and C_{dl} were discrete passives for the benchtop test; *in vivo* values were estimated from the stimulation voltage at known current output by using the initial IR drop and initial slope of capacitive charging. Q_{pulse} (similar to 'charge per phase' in biphasic systems), E_{pulse} , and $P_{stimulation}$ were calculated from measured stimulation voltage, R_{soln} and C_{dl} .

The values in the table should be taken as approximate. This is because acoustic hydrophone measurements were taken in a separate experiment from the mote operation and rely on the assumption that the mote was positioned at the point of maximal acoustic intensity. While the alignment procedure of the mote was designed to position the mote at the position of maximal acoustic intensity, this was difficult to verify, and an error of up to 20% is possible. In addition, hydrophone measurements could not be made *in vivo* and absorption through tissue had to be modeled to yield an estimate of acoustic intensity

inside the animal. Thus, the acoustic intensity values estimated at the mote were subject to the assumptions and material property inaccuracies of that model.

It should also be noted that at low PRFs, the overall efficiency was low because the total $P_{\text{stimulation}}$ was low and the device charged up quickly and remained ‘idle’ for most of the time between stimulation pulses. Under low PRF conditions, it was shown that the device could be intermittently powered up for each pulse to reduce the overall ultrasound emitted. If optimized for this application, the mote could have a small C_{store} to reduce startup time.

Table 1: System power performance

	Benchtop high PRF	<i>In vivo</i> low PRF
acoustic medium	ultrasound gel	gel, skin, muscle
mote depth from ext. txdr	48 mm	18 mm
Stimulation protocol		
specified PRF	2380 Hz	.222 Hz
specified stim current	400 μA	400 μA
specified stim pulse width	72 μs	172 μs
specified interphase gap	10 μs	80 μs
External transceiver		
external transducer	25.4 mm \emptyset	12.7 mm \emptyset
V_{TX}	28.9 V	24.8 V
U/S duty cycle with UFI's	76%	100%
$P_{\text{electrical}}$ drive ext. txdr	2.0 W	1.34 W
I_{SPTA} derated	723 mW/cm ²	713 mW/cm ²
P_{acoustic} focal plane 1 cm rad.	20.8 mW	14.6 mW
P_{acoustic} on mote piezo face	4.3 mW	2.8 mW
Mote		
mote C_{store}	4 μF	4 μF
V_{DD} steady state at low PRF	3.0 V	3.0 V
V_{DD} steady state at max PRF	1.9 V	
P into C_{store} at 1.2 V_{DD}	451 μW^*	294 μW
P into C_{store} at 1.9 V_{DD}	147 μW^*	96 μW
P into C_{store} at 2.5 V_{DD}	103 μW^*	67 μW
P into C_{store} at 3.0 V_{DD}	14.9 μW^*	9.7 μW
η acoustic -> C_{store} at 1.2 V_{DD}		10.5%
η acoustic -> C_{store} at 1.9 V_{DD}		3.4%
η acoustic -> C_{store} at 2.5 V_{DD}		2.4%
η acoustic -> C_{store} at 3.0 V_{DD}		0.34%
Load		
load R_{soln} (est. for <i>in vivo</i>)	3 k Ω	4.4 k Ω
load C_{dl} (est. for <i>in vivo</i>)	22 nF	17.9 nF

Q_{pulse}	24 nC	43.4 nC
E_{pulse}	37 nJ	108 nJ
$P_{\text{stimulation}}$	89 μ W	24 nW

* these power values were derived based on the incident acoustic power at the mote face and the measured efficiencies at various V_{DDs} .

3.3. Motes could operate in up to $\pm 25^\circ$ angular misalignment when powered by a single external transducer

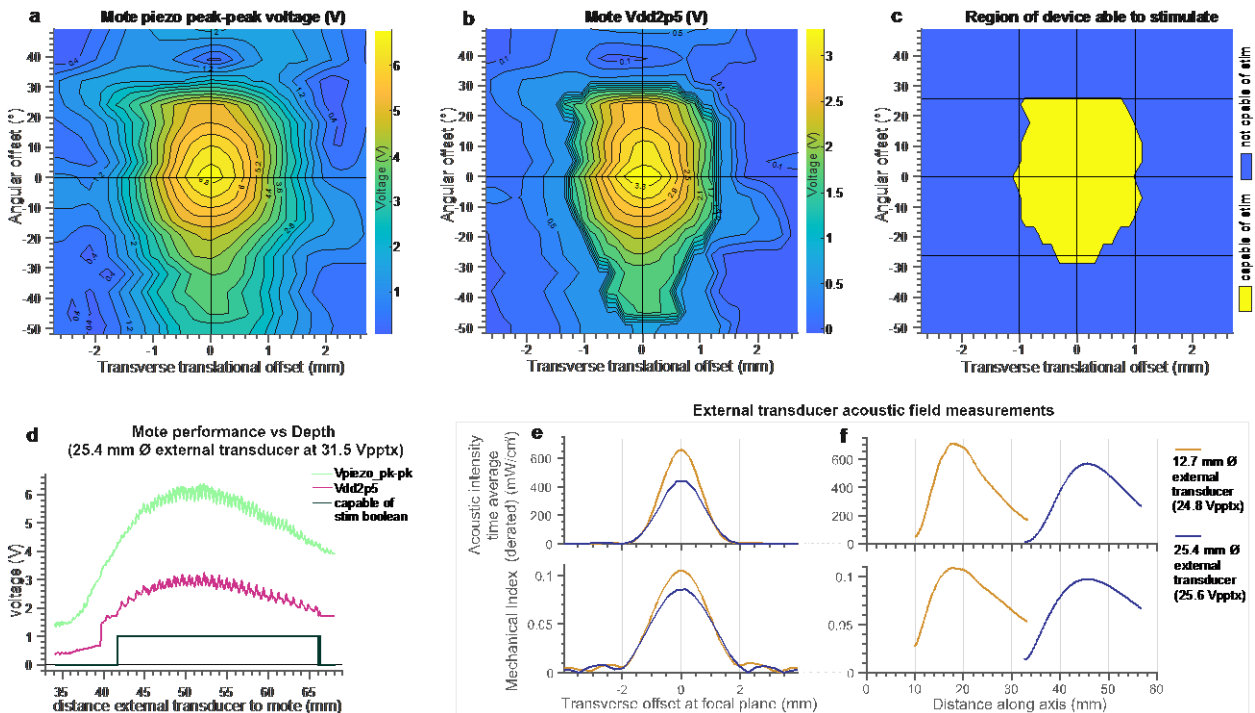


Figure 6: Profile of system performance as a function of misalignment of the acoustic link: (a, b, c) A mote was scanned in transverse offset and angular offset relative to boresight on-axis aligned with a fixed external transducer acoustic field. (a) depicts mote piezo harvest voltage. (b) depicts mote regulated voltage. (c) depicts whether the mote was able to stimulate. (d) A mote was scanned along axis (in depth) relative to a fixed external transducer acoustic field, yielding a viable region in depth. (e, f) Characterization of the external transducer acoustic field for two transducers optimized for shallow and deep usage. Data for (a,b,c,d) taken in ultrasound gel with external transducer and mote. Data for (e, f) taken a water tank with external transducer and hydrophone.

The mote is operational under ± 1.05 mm translational and $\pm 26^\circ$ angular misalignment relative to the external transducer acoustic beam. (a) Peak-peak voltage seen at the mote piezo. (b) Harvested and regulated voltage on the mote. (c) Region of full operation of the mote. (d) Mote performance as a function of depth (fully-functioning maximum depth achieved with another in-vitro device: 70 mm). All data for this figure taken in-vitro in an ultrasound gel acoustic medium with acoustic properties similar to that of water, with external transducer driving amplitude of 25 Vpk-pk in (a,b,c) and 31.5 Vpk-pk in (d).

Figure 6(a-d) depicts the acoustic link alignment range under which a mote could power-up and stimulate. The acoustic field produced by the external transducer is depicted in figure 6(e-f). The 25.4 mm diameter external transducer was used for the misalignment results reported in figure 6(a-d). Lateral misalignment (x-axis in figure 6(a-c)) of the mote relative to the central axis of the external transducer acoustic field produced a viable range of +/- 1.1 mm. Angular misalignment of the mote relative to boresight alignment with the external transducer field (y-axis in figure 6(a-c)) produced a viable range of +/- 25°. At the center of the viable range, V_{pk-pk} piezo was 6.98 V and V_{DD} was 3.47 V, and at the margin V_{pk-pk} piezo was approximately 4.3 V and V_{DD} was approximately 1.8 V. The piezo peak-peak voltage and V_{DD} showed a null at ~+40°, likely due to interaction between wavefronts incident on the top and side faces of the mote. There was no null at -40°. This may have been due to the slight asymmetry of the mote assembly (though the mote piezo is symmetric) and may have been contributed to by an artifact of the testing setup whereby a thin strand of paraffin film was used to secure the mote to the testing setup, which may have interfered with the incident wavefront. Distance alignment (figure 6(d)) of the mote relative to the face of the external transducer produced a viable range of between 41.7 mm to 66.2 mm with the 25.4 mm diameter external transducer and an estimated viable range of between 14 mm to 25 mm with the 12.7 mm diameter external transducer. Motes at depths less than 66.2 mm which do not fall into these depth ranges can be operated by placing the external transducer at the right distance with a stand-off.

3.4. Motes could operate up to 7 cm deep ex vivo communicating with a single external transducer with a focal depth of 4.8 cm

The maximum depth of operation was demonstrated to be 70 mm while maintaining full mote operation and stimulation. This used an ultrasound gel acoustic medium and the 25.4 mm diameter external transducer. Attenuation in body tissues is greater than that of ultrasound gel, reducing the maximum depth of operation. In fat tissue (1.1 dB/cm @ 1.85 MHz [56]), the maximum depth of operation is estimated to be 62 mm, in liver tissue (1.7 dB/cm @ 1.85 MHz), it is estimated at 56 mm, and in muscle tissue (2.2 dB/cm @ 1.85 MHz [58] - similar to that of castor oil sometimes used as an ultrasound phantom [59]), it is estimated at 51 mm. We use this last, more conservative, value as our depth metric. These distances can be improved by using an external transducer with longer focal length and larger diameter.

3.5. In vivo, implanted motes elicited sciatic nerve compound action potentials

Robust and repeatable *in vivo* stimulation was achieved across four motes. Two of the motes had overlaying tissue flaps replaced and sutured after implantation and were operated through-tissue (video S1). The EMG recordings taken during in-vivo trials showed the expected recruitment of compound muscle action potentials, indicating elicitation of sciatic nerve compound action potentials. For *in vivo* experiments, the 12.7 mm diameter external transducer was used at a transmit voltage of 24.8_{pk-pk},

corresponding to a derated I_{SPPA} and I_{SPTA} of 713 mW/cm^2 and mechanical index of 0.11, both below the FDA limits of 720 mW/cm^2 and 1.9, respectively, for ultrasound diagnostic imaging. Signals transmitted through tissue were similar to those through only ultrasound gel, indicating no problems from scattering or dispersion through the tissue.

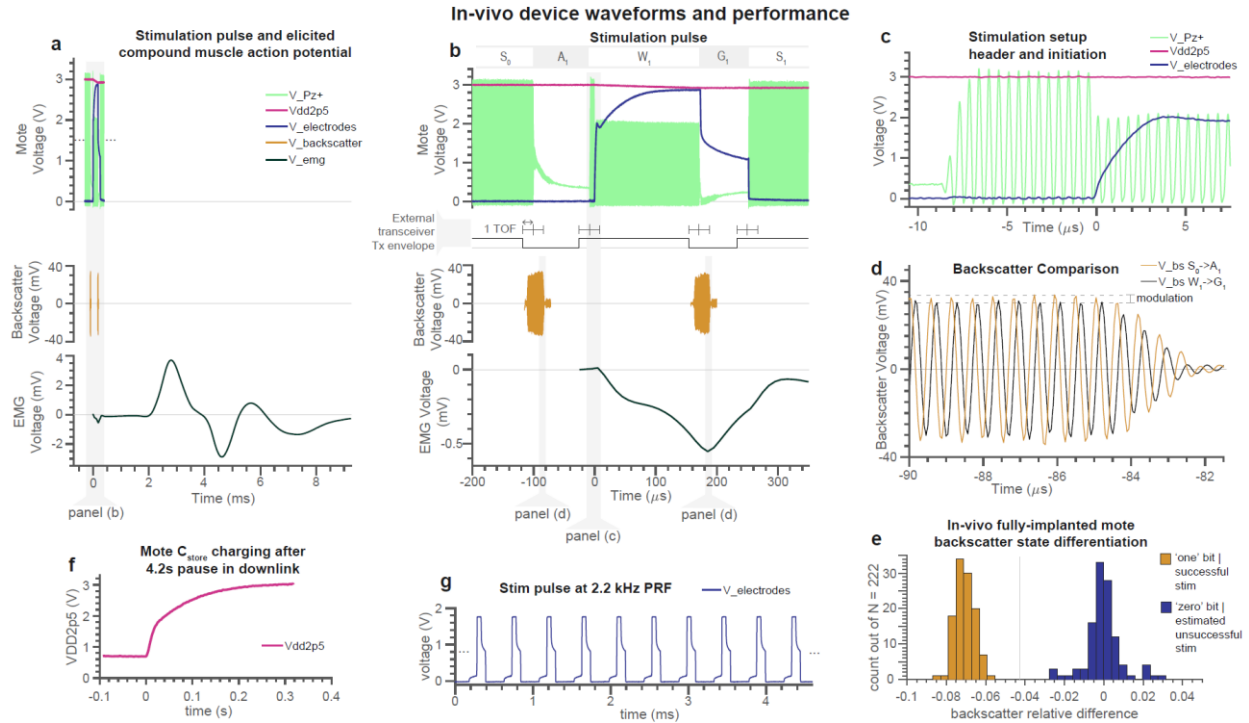


Figure 7: In-vivo performance; Mote, backscatter, evoked neural response waveforms for fully-implanted mote: (a) A stimulation pulse from the mote (top) leads to a compound muscle action potential (bottom) with a delay of approximately 2 ms. (b) Zoom-in of stimulation pulse: (top) The V_{Pz+} signal shows the incoming ultrasound signal on-off keyed downlink code, as well as modulation of the piezo during stimulation. The stimulation pulse which elicits the CMAP seen in panel (a) is specified by regions A_1 , W_1 , and G_1 . The electrode voltage shows a characteristic IR rise and capacitive charging during the current drive, then capacitive discharging during the interphase gap, and a drop at the shorting phase. The mote energy storage voltage (V_{Dd2p5}) shows a small drop during stimulation; this is topped-off during the shorting phase. Below the Mote voltage axis, the timing of the ultrasound protocol as measured at the external transceiver is depicted. This shows the acoustic time of flight (TOF) delay from the external transceiver to the mote and from the mote back to the external transceiver. (middle) The backscattered signal from the mote is captured by the external transceiver at the end of the short phase and the end of the stim phase. These two regions are compared (see panel d) to determine modulation state (see panel e). (bottom) The stimulation pulse creates an electrical artifact at the EMG electrodes. (c) At the beginning of the stim phase, 16 cycles are counted to prevent any false stim events. (d) The two backscatter regions show amplitude modulation, indicating a successful stimulation pulse. (e) In-vivo closed surgical site backscatter relative difference for 111 successful stimulation pulses and 111 estimated unsuccessful pulses. The successful stim population is calculated as the relative difference the post-short backscatter capture of pulse n and the post-stim backscatter capture of pulse n . The estimated unsuccessful stim population is calculated by comparing the post-short phase of pulse n to the post-short phase of pulse $n+1$. (f) The initial charge-up of the $4 \mu\text{F } C_{\text{store}}$ after the mote had been without power for 4.2 seconds and V_{Dd2p5} had drained to 0.7 V. (g) High pulse repetition frequency in-vivo stimulation. (note) Data in panels (a-e) are from the same stimulation parameters condition during a single in-vivo experiment with a fully implanted mote. Data in panel (f) is from in-vivo fully-implanted mote. Data in panel (g) is from in-vivo while taking data with an open surgical site.

Figure 7(a-d) shows all signals of interest during a stimulation pulse while a fully implanted mote was operated through skin and muscle layers. The downlink commands received by the mote, S_0 , A_1 , W_1 , G_1 , S_1 , can be seen in the V_{pz+} trace in figure 7(b), top. During S_0 the ultrasound envelope was high (V_{pz+}), the charge in the energy storage capacitor was topped off (V_{DD}), and the electrodes were shorted (V_{elec}). One acoustic time-of-flight (TOF, approximately 16.9 μs in this trial) before the mote saw a transition from $S_0 \rightarrow A_1$, the external interrogator set the downlink ultrasound envelope from on to off (figure 7(b), *External transceiver Tx envelope*), and after a short delay, began to capture the backscatter signal $x_{S,0}$ from the mote from the S_0 period (figure 7(b), middle). At the mote $S_0 \rightarrow A_1$ transition, the mote piezo rang down and the stimulation current amplitude TDC decoder was initiated during this first ultrasound-free interval (UFI). One TOF after the mote $S_0 \rightarrow A_1$ transition, the primary backscatter from the mote S_0 region as seen at the external transducer ceased (figure 7(d), orange line). At the mote $A_1 \rightarrow W_1$ transition, the stimulation amplitude was set, and a setup sequence lasted for 16 ultrasound cycles (figure 7(c)), after which the stimulation pulse began and M_{mod} turned on, reducing the amplitude of $V_{pz+/-}$. The voltage measured at the stimulation electrodes showed an immediate $I_{stim} \cdot R_{soln}$ increase, and then gradually increased due to charging of the double layer capacitance. V_{DD} dropped linearly during this period due to constant current flow through the stimulation electrodes. In addition, there was an electrical stimulation artifact on the EMG signal during the stimulation event (figure 7(b), bottom). One TOF before the mote $W_1 \rightarrow G_1$ transition, the external transceiver set the ultrasound envelope from on to off and after a short delay, began to capture the backscatter signal $x_{W,1}$ from the mote from the W_1 period (figure 7(b), middle). At the mote $W_1 \rightarrow G_1$ transition, the second ultrasound-free interval began at the mote, and the stimulation electrodes were set to open circuit for the interphase gap. The electrode voltage showed an immediate $I_{stim} \cdot R_{soln}$ drop and then a $R_{soln} \cdot C_{dl}$ discharge as the double-layer capacitance discharged. One TOF after the mote $W_1 \rightarrow G_1$ transition, the primary backscatter seen at the external transceiver from the W_1 period ceased (figure 7(d), black line). At the mote $G_1 \rightarrow S_1$ transition, the ultrasound envelope turned on once again and the stimulation electrodes were shorted to discharge any remaining charge. The stimulation pulse produced by this sequence of events evoked the compound muscle action potential seen in figure 7(a), bottom. The conduction delay between stimulation and evoked CMAP of approximately 1.5 ms corresponded to the expected conduction velocity of approximately 25 m/s [60] and distance of approximately 30 mm.

3.6. In vivo implanted motes backscatter communicated reliably with a BER of 1.5×10^{-7}

To characterize *in vivo* telemetry, backscatter modulation was detected as described above. Figure 7(d) shows the time-domain comparison of the backscatter signal $x_{S,0}$ from the mote at the end of S_0 (M_{mod} off) and $x_{W,1}$ from the end of W_1 (M_{mod} on). The relative difference between the L1 norms of these two regions

was calculated for 111 successful *in vivo* stimulation pulses (figure 7(e) left population). The relative difference between the L1 norms of the S_n and S_{n+1} backscatter regions was calculated for the same 111 pulses (figure 7(e) right population) and was used as an estimate of the backscatter when M_{mod} does not turn on during the W phase (which is the case during unsuccessful stim pulses). With a threshold of -0.0455, the actual BER was zero out of 222 and a gaussian fit of the distributions yielded a predicted BER of 1.5×10^{-7} . Utilizing a running average of 3 stimulation pulses reduced this to 2.1×10^{-11} . The clear separation between these two populations indicated a robust 1-bit data uplink that could reliably report to the user whether or not each pulse is successful.

3.7. *In vivo*, the system could precisely control stimulation current and pulse width to grade recruitment of compound action potential

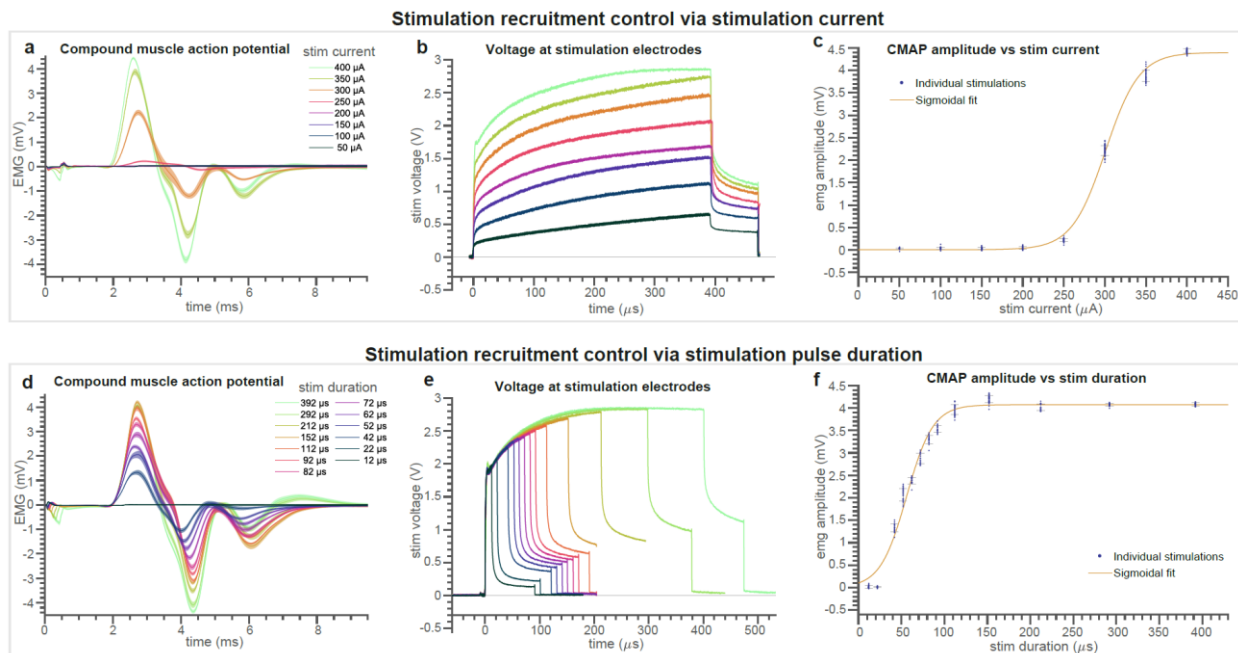


Figure 8: Precise control of evoked neural response achieved through varying stimulation current or stimulation pulse width: This data was taken with an open surgical site. **[Current-control]:** Stimulation current is varied from 50 μA to 400 μA with stimulation pulse width held at 392 μs . **(a)** CMAP waveforms show activation for 250 μA to 400 μA . Shaded error regions are $\pm 1\sigma$. **(b)** Stimulation electrode voltage shows an approximately linear trend with stimulation current. **(c)** CMAP amplitude vs. stim current showing a typical sigmoidal recruitment curve. Line is sigmoidal fit and error bars are $\pm 1\sigma$. **[Pulse-width-control]:** Stimulation pulse width is varied from 12 μs to 392 μs with stimulation current held at 400 μA . **(d)** CMAP waveforms show activation from 42 μs to 392 μs . Shaded error regions are $\pm 1\sigma$. **(e)** Stimulation electrode voltage showing similar dynamics for increasing stimulation pulse width. **(f)** CMAP amplitude vs. stim pulse width showing a typical sigmoidal recruitment curve. Line is sigmoidal fit and error bars are $\pm 1\sigma$.

Figure 8(a-c) shows the results of *in vivo* recruitment of the CMAP EMG response as stimulation current was varied from 50 μA to 400 μA while stimulation pulse width was held at 392 μs . Each condition consisted of between 30 and 60 pulses. The width of the lines in figure 8(a) and 8(d) correspond to the

standard deviation of the population of CMAP's for each stimulation condition at each time point in the trace; this showed highly repeatable stimulation and biological response across pulses. Figure 8(b) shows the measured voltage across the electrodes during stimulation. Each step is from a single stimulation event and corresponds to one of the 8 levels of stimulation current, with the voltage response increasing roughly linearly with current. At the highest stimulation current (400 μA), the stimulation voltage was compliance limited at the end of the stimulation pulse. The recruitment curve as a function of stimulation current (figure 8(c)) showed a threshold of activation between 200 μA and 250 μA and saturation between 350 μA and 400 μA . The CMAP amplitude saturated at 4.4 mV.

Figure 8(a-c) shows the results of *in vivo* recruitment of the CMAP EMG response as stimulation pulse width was varied while current was held at 400 μA . The EMG response (figure 8(d)) showed little or no CMAP response at pulse widths of 22 μs or less, and similar CMAP shapes of increasing amplitudes at pulse widths above 22 μs . Notably, the duration of the electrical artifact increased with increasing stimulation pulse width, but the time-course of the CMAP did not appreciably change, with only amplitude differing. The stimulation electrode voltages (figure 8(e)) showed that increased pulse width yielded an increasing width and peak voltage as the double-layer capacitance charged to higher voltages. The traces at the highest two pulse width values showed that at maximum current (400 μA), the stimulation voltage reached and is limited by the supply voltage of the chip. The CMAP amplitude response showed the duration-threshold of elicitation of action potential at 400 μA current to be approximately 26 μs , with response saturation around 150 μs and maximum CMAP amplitude of 4.2 mV.

A second set of current-control and pulse-width-control sweeps were performed two hours after the first (figure S1). Wireless link performance, communications, and stimulation output were unchanged. The biological response was very similar but showed slight changes to the CMAP recruitment curves. The recruitment curves shifted left, showing a reduced threshold of recruitment of approximately 15%, and saturated at approximately 11% lower maximum CMAP amplitude. These slight differences were potentially due to changes in impedance at the electrodes and excitability in the nerve as the tissue began to respond to the implant, and possibly muscle fatigue even though pulse repetition frequency was low.

3.8. The system produced pulses from 0.25 Hz to 2.2 kHz, yielding four regimes of muscle activation

In vivo stimulation was performed at pulse repetition frequencies of: [0.22, 0.33, 1, 2, 5, 10, 32, 100, 320, 2000, 2222] Hz, with some compliance limiting at the higher PRF's. Pulse width was 52 μs and current was set to 400 μA . By visually observing muscle twitch response, we qualitatively reported single twitches at 0.25, 0.33, 1, 2, 5, and 10 Hz, unfused tetanus at 32 Hz and fused tetanus at 100 and 320 Hz. This matched expected muscle responses for rat gastrocnemius [61]. At 2 kHz and 2.22 kHz (figure 7(g)), we observed a single initial twitch and then apparent relaxation. While we did not measure muscle force in this study

and thus could not positively confirm nerve block, nerve block has been reported at 2 kHz stimulation frequency and 1 V drive voltage (approximately 666 μ A) [62]. Thus, while not conclusive, these observations were consistent with the system performing nerve block.

4. Discussion

4.1. The system demonstrated a practical implementation of an ultra-small ultrasonic wireless neural stimulator

Our results indicated that precise, controlled compound action potentials can be elicited by the StimDust system. This reliable and controllable stimulation throughout the range of the nerve recruitment curve was critical for safe and efficacious stimulation. Furthermore, miniaturization of the precision controllable stimulator enabled placement of the device directly at the stimulation site *on* the sciatic nerve.

Table 2 summarizes the performance of the StimDust system and compares with state-of-the-art implantable wireless neural stimulators. Wireless ultrasonic power and data delivery enabled implant operation at a depth of 70 mm in ultrasound gel. Additionally, direct control of the stimulation waveform by the received ultrasound boasted several advantages over state-of-the-art. Compared to systems that program motes via a bitstream, StimDust could achieve sub- μ s ($1/f_{\text{carrier}}$) temporal resolution with a larger dynamic range for pulse width, interphase gap, and PRF because the complexity is pushed to the external transceiver, which had fewer computational and power constraints. The stimulators which used only passive components ([30] and [31]) use a direct control scheme as well; however, the stimulation intensity was dictated by the received power and both used voltage stimulation which is sensitive to electrode properties. Furthermore, they did not feature an uplink whereas StimDust had a wireless uplink via ultrasonic backscatter for safety monitoring and alignment. Active rectification increased efficiency and established a ground reference potential, enabling StimDust to use passive recharge to save power relative to biphasic stimulation while safely clearing residual stimulation charge on the electrodes, which other direct control systems ([30], [31]) were unable to do. Using an enable signal, or stimulation start command, meant the mote can stimulate with very low latency, which is crucial for closed-loop experimentation.

In addition to highly programmable stimulation, StimDust was also the smallest implementation of a neural stimulator with precise current-control output. Via efficient integration and co-design of the piezocrystal, StimDust IC, storage capacitor, and interface electrodes, the StimDust mote was just 2.2 mm³ in volume and 10mg. This represents >10x improvement in depth/volume figure of merit (FoM) and >25x improvement in volume/efficiency FoM relative to other state-of-the-art precision neural stimulators.

Table 2: State-of-the-art comparisons table

	TBioCAS '18 [40]	TCAS II '13 [39]	PLOS ONE '17 [30]	Sci. Reports '18 [33]	Front. Neuro. '17 [31]	StimDust
Stim. type	current	current	voltage	current	voltage	current
Link	ultrasound	ultrasound	RF	4 coil inductive	RF	ultrasound
f_{carrier} [MHz]	1.3	1	2400	13.56	10	1.85
Uplink	none	none	none	433 MHz OOK	none	backscatter
Process [nm]	180HV	350	discrete	130	discrete	65
Waveform configuration	digital bitstream	digital bitstream	received power	digital bitstream	received power	envelope detection
F_{stim} [Hz] / resol. [bit]	0 - 60	60 - 265 / 2b	0 - 25*	13-414 / 5b	2*	0 - 5k**
Stim start	enable signal	--	received power	stim command	received power	enable signal
T_{pulse} resolution [us]	14 / 5b	200 / fixed	continuous	9.5 / 5b	continuous	continuous
$I_{\text{stim,max}}$ [μ A] / resol. [bit]	5000 / 8b	640 / 5b	undefined	1860 / 5b	undefined	400 / 3b
T_{gap} resolution [μ s]	$1/2 T_{\text{pulse}}$	--	N/A	9.5 / 5b	N/A	continuous
Charge balance	biphasic/gnd	dc-blocking cap	none	3b biphasic correction	none	passive recharge
Compliance voltage (V)	15	3.3	N/A	2	N/A	3
Animal model	ex-vivo frog leg					
	sciatic	rat abdomen	pig vagus	rat sciatic	rat sciatic	rat sciatic
Fully-implanted	no	no	yes	yes	yes	yes
in-vitro depth _{tx-rx} [mm]	105	--	--	--	--	70
in-vivo depth _{tx-rx} [mm]	--	50	15	--	50	20
Mass [mg]	78	--	300	2800	--	10
Circuit η ($P_{\text{stim}}/P_{\text{in}}$) [%]	<50	--	20	--	--	82
Volume [mm ³]	39	1020	40.5 [†]	2250	0.45 [‡]	2.2[‡]
Electrodes [mm]	0.50 x 2.0 Pt cylinder	--	2.70 x 1.0 Pt cuff	cuff	0.30 Pt disk	0.55 PEDOT square
Implant encapsulation	PDMS	--	epoxy	epoxy & PDMS	epoxy	parylene
FOM (Depth/Volume)	2.69	0.05	0.37	--	111.11	31.82
FOM (Volume/Efficiency)	0.78	--	2.03	--	--	0.03
*demonstrated						*includes stim electrodes
[†] estimated						**up to 16kHz in burst

4.2. A wide ultrasound acceptance angle of the piezo was important to lessen constraints on mote implantation and external transceiver positioning:

The use of an ultrasonic link over an RF one was crucial for achieving much higher link efficiencies at sub-mm sizes in tissue. A major consideration for the practical deployment of a system in the body with an ultrasonic link is ensuring that the mote is properly placed and oriented within the acoustic field generated by the external transceiver. Link operation under non-ideal positioning and orientation is a well-understood aspect of RF-based systems; while some analysis and nondimensional parameters on the matter has been developed for acoustic communications links [63], it is vitally important to assess this aspect of fully implemented systems. With the present system, a mote could be operated when it was shallower than 63 mm in tissue, the incident ultrasound was within a 50° range around the mote central axis, and the external beam was centered within a 2.1 mm range around the mote position. The most important metric is the large acceptance angle of the mote piezo because it allowed a strong link even if the mote's orientation was non-optimal (not boresight with respect to the external transducer). While it is relatively easy to change the lateral position of an external transducer to correct for lateral offsets in an acoustic link, it is very difficult to change the orientation of a mote after implantation. Thus, a mote with a wide acceptance angle takes care of moderate mote angular misalignment and adjustment of the

external transducer can take care of lateral misalignment. The 2.1 mm lateral range allowed robustness to small lateral misalignment and motion. Translating or angling the external transducer could compensate for greater lateral misalignment. In a future system, a beamforming external transducer array can be designed to electronically perform this function and continuously keep the mote within the 2.1 mm central range of the beam. In new designs of acoustically linked microimplantables, a piezo thickness-to-width aspect ratio of 1 or greater should achieve a similarly wide acceptance angle, ensuring that precise mote orientation during implantation is not a major constraining factor.

4.3. Stimulation was due to the mote output current and was not directly ultrasound mediated

At 1.85 MHz, the threshold of ultrasound-mediated neural stimulation has been reported at approximately 10 W/cm² pulse-average intensity [64]; this is more than 14x higher intensity than that used in this study. Furthermore, as the system increased stimulation current from 50 μ A to 400 μ A with a corresponding recruitment of CMAP response, acoustic power was nearly identical and actually decreased slightly since the protocol utilizes a longer TDC gap when specifying high current. Additionally, no EMG response was observed when the system was driven with continuous ultrasound at the same intensity as used for controlling the device, but with no coded downlink signals. Finally, a pilot *in vivo* experiment, which powered the mote electrically with no ultrasound, produced stimulation and evoked CMAP's as expected. Utilizing a current-control implantable stimulator provides improved stimulation accuracy and spatial precision over directly mediated ultrasonic stimulation, and requires substantially lower acoustic intensities and thus has lower risk from ultrasound-induced thermal or cavitation damage [65].

4.4. High power-efficiency is important for high-PRF use-cases; high voltage-efficiency is important for low PRF use-cases

As demonstrated by this system, for cm-scale depths and low mm- to micro-scale devices, ultrasound at safe intensity levels was able to generate $\sim 7 V_{pk-pk}$ piezo and $\sim 3.5 V$ rectified voltage with an ultrasonic wireless link. This is sufficient voltage for stimulation with low-impedance electrodes and most other functions that a similar micro-implantable may perform. Therefore, we chose to optimize power harvesting for power efficiency rather than voltage efficiency. This enabled our high PRF, which is important for some clinical use cases such as nerve block. Our system was voltage-limited at low PRF's and was only power-limited at higher PRFs in the 100's of Hz or greater (or high total $P_{stimulation}$). For devices that push scaling to mid- μ m scale or increase to >10 cm depth while maintaining low-mm to high- μ m scale, the voltage generated by the piezo will be substantially lower. These devices will have to sacrifice power efficiency for voltage efficiency, which is a reasonable trade-off if high PRF is not important. A similar system with a voltage-doubling charge pump may be able to operate at low PRF under $\frac{1}{4}$ the

incident acoustic power, enabling a thinner piezo and smaller device or multiple centimeters greater depth of operation.

4.6. The low minimum acoustic intensity for operation of the system opens up the use case of wireless transcranial CNS neural stimulator, including DBS and brain-machine interface applications

The high efficiency design of the mote enabled operation in settings where acoustic intensity was as low as 142 mW/cm^2 . This opens up new use cases such as placing the mote in the brain and establishing an ultrasonic power and communications link through the skull.

While the skull is more attenuating to ultrasound than are soft tissues, transcranial ultrasound has been used for both diagnostic and therapeutic purposes and has been shown to safely achieve ultrasonic power levels in the brain which are sufficient for the the StimDust mote to function. In one study in humans ([66]), 2 MHz ultrasound was transmitted through the temporal bone with a focal depth of 4.5 cm. This system had an estimated focal pressure amplitude of 70 kPa [67] and acoustic intensity of 159 mW/cm^2 . Correcting for the frequency-dependent acoustic attenuation in bone ([68]), this is an estimated 279 mW/cm^2 at 1.85 MHz. A different study utilizing a transcranial ultrasound system designed for humans at 220 kHz ([69]) reported up to an estimated 215 W/cm^2 at deep brain focal points while keeping superficial skull and skin tissues below thermal thresholds. This is an estimated focal intensity of 480 mW/cm^2 at 1.85 MHz. Thus, the StimDust mote, needing 142 mW/cm^2 to operate, is well within the power limits of existing safe transcranial ultrasound systems.

5. Conclusion

We have introduced the smallest wireless neural stimulator that can deliver safe and controllable stimulation. Compact mote integration and programmable stimulation is enabled by a custom wireless ultrasound protocol and an energy efficient integrated circuit. We demonstrated its use fully implanted in anesthetized rats to controllably elicit compound action potentials across a range of clinically relevant stimulation regimes. Taken together, this work shows a practical demonstration of a stimulator for the PNS with clear applicability to CNS applications. We anticipate the debut of a new class of neural stimulators that are small enough to be deployed en masse with low risk to the patient, and which open up new and powerful therapeutic and neural interface techniques.

References

- [1] K. Chakravarthy, A. Nava, P. J. Christo, and K. Williams, "Review of Recent Advances in Peripheral Nerve Stimulation (PNS)," *Curr. Pain Headache Rep.*, vol. 20, no. 11, 2016.
- [2] R. P. Michelson, "Electrical Stimulation of the Human Cochlea: A Preliminary Report," *Arch. Otolaryngol. - Head Neck Surg.*, vol. 93, no. 3, pp. 317–323, Mar. 1971.
- [3] K. Birmingham *et al.*, "Bioelectronic medicines: A research roadmap," *Nat. Rev. Drug Discov.*, vol. 13, no. 6, pp. 399–400, 2014.
- [4] D. T. T. Plachta *et al.*, "Blood pressure control with selective vagal nerve stimulation and minimal side effects," *J. Neural Eng.*, vol. 11, no. 3, 2014.
- [5] F. A. Koopman, S. S. Chavan, S. Miljko, S. Grazio, S. Sokolovic, and P. R. Schuurman, "Vagus nerve stimulation inhibits cytokine production and attenuates disease severity in rheumatoid arthritis," vol. 113, no. 29, 2016.
- [6] T. M. Bruns, D. J. Weber, and R. A. Gaunt, "Microstimulation of Afferents in the Sacral Dorsal Root Ganglia Can Evoke Reflex Bladder Activity," *NeuroUrol Urodyn.*, vol. 34, pp. 65–71, 2015.
- [7] L. L. Zimmerman, I. C. Rice, M. B. Berger, and T. M. Bruns, "Tibial Nerve Stimulation to Drive Genital Sexual Arousal in an Anesthetized Female Rat," *J. Sex. Med.*, vol. 15, no. 3, pp. 296–303, 2018.
- [8] D. W. Tan, M. A. Schiefer, M. W. Keith, J. R. Anderson, J. Tyler, and D. J. Tyler, "A neural interface provides long-term stable natural touch perception," *Sci. Transl. Med.*, vol. 6, no. 257, 2014.
- [9] A. B. Ajiboye *et al.*, "Restoration of reaching and grasping movements through brain-controlled muscle stimulation in a person with tetraplegia: a proof-of-concept demonstration," *Lancet*, vol. 389, no. 10081, pp. 1821–1830, 2017.
- [10] B. Bonaz, V. Sinniger, and S. Pellissier, "The vagus nerve in the neuro-immune axis: Implications in the pathology of the gastrointestinal tract," *Front. Immunol.*, vol. 8, no. NOV, 2017.
- [11] A. L. Benabid *et al.*, "Long-term suppression of tremor by chronic stimulation of the ventral intermediate thalamic nucleus," *Lancet*, vol. 337, no. 8738, pp. 403–406, 1991.
- [12] P. Riva-Posse *et al.*, "A connectomic approach for subcallosal cingulate deep brain stimulation surgery: prospective targeting in treatment-resistant depression," *Mol. Psychiatry*, vol. 23, no. 4, pp. 843–849, 2017.
- [13] A. S. Widge, D. A. Malone, and D. D. Dougherty, "Closing the loop on deep brain stimulation for treatment-resistant depression," *Front. Neurosci.*, vol. 12, no. MAR, pp. 1–10, 2018.
- [14] G. K. Bergey *et al.*, "Long-term treatment with responsive brain stimulation in adults with refractory partial seizures," 2015.
- [15] A. Ramirez-Zamora *et al.*, "Evolving applications, technological challenges and future

- opportunities in neuromodulation: Proceedings of the fifth annual deep brain stimulation think tank," *Front. Neurosci.*, vol. 11, no. JAN, 2018.
- [16] S. R. Santacruz, E. L. Rich, J. D. Wallis, and J. M. Carmena, "Caudate Microstimulation Increases Value of Specific Choices," *Curr. Biol.*, vol. 27, no. 21, p. 3375–3383.e3, 2017.
- [17] M. L. Settell *et al.*, "Functional circuitry effect of ventral tegmental area deep brain stimulation: Imaging and neurochemical evidence of mesocortical and mesolimbic pathway modulation," *Front. Neurosci.*, vol. 11, no. MAR, pp. 1–11, 2017.
- [18] A. Najarpour Froushani, C. C. Pack, and M. Sawan, "Cortical visual prostheses: From microstimulation to functional percept," *J. Neural Eng.*, vol. 15, no. 2, 2018.
- [19] R. E. Hampson *et al.*, "Facilitation of memory encoding in primate hippocampus by a neuroprosthesis that promotes task-specific neural firing," *J. Neural Eng.*, vol. 10, no. 6, 2013.
- [20] K. W. Ter Horst *et al.*, "Striatal dopamine regulates systemic glucose metabolism in humans and mice," *Sci. Transl. Med.*, vol. 10, no. 442, pp. 1–11, 2018.
- [21] S. Venkatraman and J. M. Carmena, "Active sensing of target location encoded by cortical microstimulation," *IEEE Trans. Neural Syst. Rehabil. Eng.*, vol. 19, no. 3, pp. 317–324, 2011.
- [22] J. E. O'Doherty, M. A. Lebedev, T. L. Hanson, N. A. Fitzsimmons, and M. A. L. Nicolelis, "A brain-machine interface instructed by direct intracortical microstimulation," *Front. Integr. Neurosci.*, vol. 3, no. 13, pp. 3662–3669, 2009.
- [23] J. E. O'Doherty *et al.*, "Active tactile exploration using a brain-machine-brain interface," *Nature*, vol. 479, no. 7372, pp. 228–231, 2011.
- [24] M. C. Dadarlat, J. E. O'Doherty, and P. N. Sabes, "A learning-based approach to artificial sensory feedback leads to optimal integration," *Nat. Neurosci.*, vol. 18, no. 1, pp. 138–144, 2015.
- [25] Medtronic, "Medtronic Activa 37601," *English*, 2008.
- [26] F. D. Time and M. Confidential, "Intellis™ Rechargeable neurostimulator Implant manual Rx only M946871A001," 2012.
- [27] "RNS® System User Manual," 2015.
- [28] E. Moro, "Neurosurgery: Complications of DBS surgery-insights from large databases," *Nat. Rev. Neurol.*, vol. 12, no. 11, pp. 617–618, 2016.
- [29] S. M. Restaino, E. Abliz, K. Wachrathit, V. Krauthamer, and S. B. Shah, "Biomechanical and functional variation in rat sciatic nerve following cuff electrode implantation," *J. Neuroeng. Rehabil.*, vol. 11, no. 1, pp. 1–10, 2014.
- [30] Y. Tanabe *et al.*, "High-performance wireless powering for peripheral nerve neuromodulation systems," *PLoS One*, vol. 12, no. 10, pp. 1–13, 2017.
- [31] D. K. Freeman *et al.*, "A sub-millimeter, inductively powered neural stimulator," *Front. Neurosci.*, vol. 11, no. NOV, pp. 1–12, 2017.
- [32] H. M. Lee, K. Y. Kwon, W. Li, and M. Ghovanloo, "A power-efficient switched-capacitor stimulating system for electrical/optical deep brain stimulation," *IEEE J. Solid-State Circuits*, vol. 50, no. 1, pp. 360–374, 2015.

- [33] B. Lee *et al.*, “An Implantable Peripheral Nerve Recording and Stimulation System for Experiments on Freely Moving Animal Subjects,” *Sci. Rep.*, vol. 8, no. 1, pp. 1–12, 2018.
- [34] Y. P. Lin *et al.*, “A Battery-Less, Implantable Neuro-Electronic Interface for Studying the Mechanisms of Deep Brain Stimulation in Rat Models,” *IEEE Trans. Biomed. Circuits Syst.*, vol. 10, no. 1, pp. 98–112, 2016.
- [35] D. Seo, J. M. Carmena, J. M. Rabaey, E. Alon, and M. M. Maharbiz, “Neural Dust: An Ultrasonic, Low Power Solution for Chronic Brain-Machine Interfaces,” *arXiv.org*, vol. q-NC, no. April, 2013.
- [36] D. Seo, J. M. Carmena, J. M. Rabaey, M. M. Maharbiz, and E. Alon, “Model validation of untethered, ultrasonic neural dust motes for cortical recording,” *J. Neurosci. Methods*, vol. 244, pp. 114–122, 2015.
- [37] D. Seo *et al.*, “Wireless Recording in the Peripheral Nervous System with Ultrasonic Neural Dust,” *Neuron*, vol. 91, no. 3, pp. 529–539, 2016.
- [38] J. Charthad, M. J. Weber, T. C. Chang, and A. Arbabian, “A mm-Sized Implantable Medical Device (IMD) With Ultrasonic Power Transfer and a Hybrid Bi-Directional Data Link,” *IEEE J. Solid-State Circuits*, vol. 50, no. 8, pp. 1741–1753, 2015.
- [39] Y. S. Luo *et al.*, “Ultrasonic power/data telemetry and neural stimulator with OOK-PM signaling,” *IEEE Trans. Circuits Syst. II Express Briefs*, vol. 60, no. 12, pp. 827–831, 2013.
- [40] J. Charthad *et al.*, “A mm-Sized wireless implantable device for electrical stimulation of peripheral nerves,” *IEEE Trans. Biomed. Circuits Syst.*, vol. 12, no. 2, pp. 257–270, 2018.
- [41] FDA, “Information for Manufacturers Seeking Marketing Clearance of Diagnostic Ultrasound Systems and Transducers,” 2008. [Online]. Available: <https://www.fda.gov/downloads/UCM070911.pdf>.
- [42] B. C. Johnson *et al.*, “StimDust : A 6.5mm³ , Wireless Ultrasonic Peripheral Nerve Stimulator with 82% Peak Chip Efficiency,” *Cicc*, pp. 8–11, 2018.
- [43] B. C. Johnson *et al.*, “An implantable 700 μ W 64-channel neuromodulation IC for simultaneous recording and stimulation with rapid artifact recovery,” *IEEE Symp. VLSI Circuits, Dig. Tech. Pap.*, pp. C48–C49, 2017.
- [44] A. C. Weitz, M. R. Behrend, M. S. Humayun, R. H. Chow, and J. D. Weiland, “Interphase gap decreases electrical stimulation threshold of retinal ganglion cells,” *Proc. Annu. Int. Conf. IEEE Eng. Med. Biol. Soc. EMBS*, pp. 6725–6728, 2011.
- [45] A. C. Weitz *et al.*, “Interphase gap as a means to reduce electrical stimulation thresholds for epiretinal prostheses,” *J. Neural Eng.*, vol. 11, no. 1, 2014.
- [46] S. Stanslaski *et al.*, “Design and validation of a fully implantable, chronic, closed-loop neuromodulation device with concurrent sensing and stimulation,” *IEEE Trans. Neural Syst. Rehabil. Eng.*, vol. 20, no. 4, pp. 410–421, 2012.
- [47] S. Venkatraman *et al.*, “In Vitro and In Vivo Evaluation of PEDOT Microelectrodes for Neural Stimulation and Recording,” vol. 19, no. 3, pp. 307–316, 2011.
- [48] C. Hassler, T. Boretius, and T. Stieglitz, “Polymers for neural implants,” *J. Polym. Sci. Part B Polym. Phys.*, vol. 49, no. 1, pp. 18–33, 2011.

- [49] J. C. Barrese *et al.*, "Failure mode analysis of silicon-based intracortical microelectrode arrays in non-human primates," *J. Neural Eng.*, vol. 10, no. 6, 2013.
- [50] H. Fang *et al.*, "Ultrathin, transferred layers of thermally grown silicon dioxide as biofluid barriers for biointegrated flexible electronic systems," *Proc. Natl. Acad. Sci.*, vol. 113, no. 42, pp. 11682–11687, 2016.
- [51] C. A. Diaz-Botia *et al.*, "A silicon carbide array for electrocorticography and peripheral nerve recording," *J. Neural Eng.*, vol. 14, no. 056006, 2017.
- [52] D. K. Piech, J. E. Kay, B. E. Boser, and M. M. Maharbiz, "Rodent wearable ultrasound system for wireless neural recording," *Proc. Annu. Int. Conf. IEEE Eng. Med. Biol. Soc. EMBS*, pp. 221–225, 2017.
- [53] H.-Y. Tang, Y. Lu, S. Fung, D. A. Horsley, and B. E. Boser, "11.8 Integrated ultrasonic system for measuring body-fat composition," in *2015 IEEE International Solid-State Circuits Conference - (ISSCC) Digest of Technical Papers*, 2015, pp. 1–3.
- [54] D. Seo *et al.*, "Ultrasonic Beamforming System for Interrogating Multiple Implantable Sensors," pp. 1–4, 2015.
- [55] R. A. Casarotto, J. C. Adamowski, F. Fallopa, and F. Bacanelli, "Coupling Agents in Therapeutic Ultrasound: Acoustic and Thermal Behavior," *Arch. Phys. Med. Rehabil.*, vol. 85, no. 1, pp. 162–165, 2004.
- [56] H. Azhari, "Appendix A: Typical Acoustic Properties of Tissues," *Basics Biomed. Ultrasound Eng.*, pp. 313–314, 2010.
- [57] N. Jiménez, J. Redondo, V. Sánchez-Morcillo, F. Camarena, Y. Hou, and E. E. Konofagou, "Nonlinear Acoustics FDTD method including Frequency Power Law Attenuation for Soft Tissue Modeling," *arXiv*, 2014.
- [58] D. K. Nassiri, D. Nicholas, and C. R. Hill, "Attenuation of ultrasound in skeletal muscle," *Ultrasonics*, vol. 17, no. 5, pp. 230–232, 1979.
- [59] M. Liebler, S. Ginter, T. Dreyer, and R. E. Riedlinger, "Full wave modeling of therapeutic ultrasound: Efficient time-domain implementation of the frequency power-law attenuation," *J. Acoust. Soc. Am.*, vol. 116, no. 5, pp. 2742–2750, 2004.
- [60] M. Ayaz *et al.*, "Sexual dependency of rat sciatic nerve fiber conduction velocity distributions.," *Int. J. Neurosci.*, vol. 117, no. 11, pp. 1537–49, 2007.
- [61] J. Celichowski, "Mechanisms underlying the regulation of motor unit contraction in the skeletal muscle," *Journal of Physiology and Pharmacology*, vol. 51, no. 1, pp. 17–33, 2000.
- [62] N. Bhadra, N. Bhadra, K. Kilgore, and K. J. Gustafson, "High frequency electrical conduction block of the pudendal nerve," *J. Neural Eng.*, vol. 3, no. 2, pp. 180–187, 2006.
- [63] D. B. Christensen and S. Roundy, "Non-dimensional analysis of depth, orientation, and alignment in acoustic power transfer systems," *Smart Mater.*, 2018.
- [64] P. P. Ye, J. R. Brown, and K. B. Pauly, "Frequency dependence of ultrasound neurostimulation in the mouse brain," *Ultrasound Med. Biol.*, vol. 42, no. 7, pp. 1512–1530, 2016.

- [65] M. E. Downs, S. A. Lee, G. Yang, S. Kim, Q. Wang, and E. E. Konofagou, "Non-invasive peripheral nerve stimulation via focused ultrasound *in vivo*," *Phys. Med. Biol.*, 2017.
- [66] A. V. Alexandrov *et al.*, "Ultrasound-Enhanced Systemic Thrombolysis for Acute Ischemic Stroke," *N. Engl. J. Med.*, vol. 351, no. 21, pp. 2170–2178, Nov. 2004.
- [67] C. Baron, J. F. Aubry, M. Tanter, S. Meairs, and M. Fink, "Simulation of Intracranial Acoustic Fields in Clinical Trials of Sonothrombolysis," *Ultrasound Med. Biol.*, vol. 35, no. 7, pp. 1148–1158, 2009.
- [68] F. J. Fry and J. E. Barger, "Acoustical properties of the human skull," *J. Acoust. Soc. Am.*, vol. 63, no. 5, pp. 1576–1590, 1978.
- [69] T. Hölscher, D. Fisher, and R. Raman, "Noninvasive Transcranial Clot Lysis Using High Intensity Focused Ultrasound," *J. Neurol. Neurophysiol.*, vol. 01, no. 01, pp. 1–6, 2011.

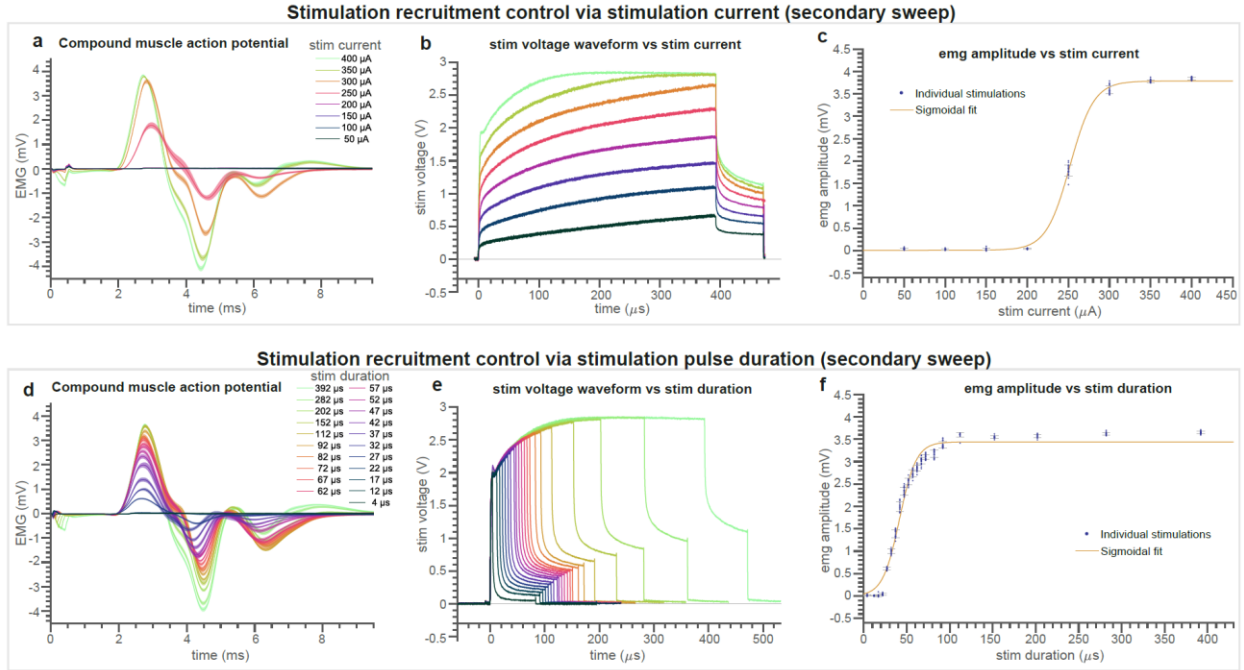


Figure S1: Evoked response stimulation current and stimulation pulse width sweep: This data was taken with the same animal and mote as in that in figure 8, but 2 hours after the first sweep. See figure 8 for panel descriptions.